APPLIED OPTICS

(60)

Aerosol retrievals over the ocean using channel 1 and 2 AVHRR data: a sensitivity analysis and preliminary results

p 4/9

Michael I. Mishchenko, Igor V. Geogdzhayev, Brian Cairns, William B. Rossow, and Andrew A. Lacis

This paper outlines the methodology of interpreting channel 1 and 2 AVHRR radiance data over the oceans and describes a detailed analysis of the sensitivity of monthly averages of retrieved aerosol parameters to the assumptions made in different retrieval algorithms. The analysis is based on using real AVHRR data and exploiting accurate numerical techniques for computing single and multiple scattering and spectral absorption of light in the vertically inhomogeneous atmosphere-ocean system. We show that two-channel algorithms can be expected to provide significantly more accurate and less biased retrievals of the aerosol optical thickness than one-channel algorithms and that imperfect cloud screening and calibration uncertainties are by far the largest sources of errors in the retrieved aerosol parameters. Both underestimating and overestimating aerosol absorption as well as the potentially strong variability of the real part of the aerosol refractive index may lead to regional and/or seasonal biases in optical thickness retrievals. The Ångström exponent appears to be the most invariant aerosol size characteristic and should be retrieved along with optical thickness as the second aerosol parameter.

OCIS codes: 010.1100, 010.1110, 010.1310, 010.7030, 280.1100, 280.1310

The authors are with the Goddard Institute for Space Studies, 2880 Broadway, New York, NY 10025. I. V. Geogdzhayev and B. Cairns are also with the Department of Applied Physics and Applied Mathematics, Columbia University, 2880 Broadway, New York, NY 10025. The e-mail address for M. I. Mishchenko is crmim@giss.nasa.gov and his fax number is 212 678 5622.

1. Introduction

The effect of tropospheric aerosols on global climate via the direct and indirect radiative forcings is one of the largest remaining uncertainties in climate change studies.[1] Current assessments of the direct aerosol radiative effect mainly focus on sulfate aerosols (e.g., Roeckner *et al.*[2]). It has become clear, however, that other aerosol types like soil dust and smoke from biomass burning and sea salt are also likely to be important climate forcing factors.[3,4] The magnitude and even the sign of the climate forcing caused by these aerosol types is still unknown. Once the global distribution of aerosol properties such as the optical thickness, size distribution, and chemical composition is available, the calculation of the direct aerosol forcing using general circulation models (GCMs) is rather straightforward.[5,6] However, estimates of the indirect aerosol effect require information on the distribution of the aerosol number density and additional knowledge of the physics and chemistry of aerosol-cloud interactions,[7] which are still poorly understood.

The retrieval of the global distribution of aerosol properties and determination of trends in its temporal variation can only be achieved using long-term satellite measurements. The standard one-channel Advanced Very High Resolution Radiometer (AVHRR) aerosol retrieval algorithm[8] uses channel 1 radiances (nominal wavelength $\lambda_1 = 0.65\mu m$) and relies on the fact that the radiance reflected by an aerosol layer over the dark ocean surface is nearly proportional to the product of the aerosol phase function $P(\Theta)$ at the observation scattering angle Θ, single-scattering albedo ϖ, and optical thickness τ. The phase function and the single-scattering albedo are, in turn, dependent on the aerosol composition and size and shape distributions and are functions of many parameters. Even in the simplest case of a monomodal polydispersion of homogeneous spherical particles, the number of unknown model parameters is at least 5: aerosol optical thickness, real and imaginary parts of the refractive index, and effective radius and effective variance of the size distribution.[9] Since the AVHRR algorithm utilizes only one datum per pixel (channel 1 reflectance at a single observation geometry), it can retrieve only one model parameter (optical thickness), whereas all remaining parameters must be fixed *a priori*. Although the choice of the latter parameters can be optimized such that the algorithm produces a minimal *long term*

statistical deviation from existing sun photometer measurements of the optical thickness,[8] the strong spatial and temporal variability of the aerosol size, shape, and composition makes inevitable large errors in the assumed phase function and thus in the retrieved optical thickness in particular cases. Such large errors have been demonstrated not only by detailed sensitivity analyses,[10–12] but also by direct comparisons of AVHRR retrievals with sun photometer measurements. For example, figure 4 of Stowe *et al.*[8] shows relative errors in the retrieved τ exceeding 100% and absolute errors exceeding 0.15. The results of Ignatov *et al.*[13] show even larger discrepancies and suggest that more detailed comparisons of single-channel AVHRR retrievals with future sun photometer measurements are likely to reveal more significant errors.

Another important limitation of the standard AVHRR algorithm is that it provides no information about the effective particle size and thus makes impossible estimates of the aerosol indirect radiative forcing. Indeed, the quantification of the Twomey effect[14] requires accurate satellite measurements of cloud condensation nuclei (CCN) column densities. The only way of retrieving the number of tropospheric aerosols in the vertical column of unit horizontal cross section from satellite radiance measurements is to divide the satellite-retrieved aerosol optical thickness τ by the average extinction cross section per particle. Since the AVHRR algorithm assumes rather than retrieves the aerosol model, the strong sensitivity of the extinction cross section to assumed aerosol effective radius and the significant temporal and spatial aerosol variability make single-channel AVHRR retrievals of the CCN column concentration highly inaccurate.[15]

It has been suggested that the use of multichannel reflectance measurements can provide additional information on the aerosol model and also improve the accuracy of the optical thickness retrieval.[16–22] In addition to channel 1 radiance data, AVHRR provides channel 2 reflectances (nominal wavelength $\lambda_2 = 0.85\mu m$) that can be used to improve the performance of the AVHRR algorithm by retrieving two aerosol parameters rather than just one. Again, one of these parameters must be the aerosol optical thickness at a visible wavelength, whereas there is, in general, a choice for the second retrieved parameter. Indeed, even if the aerosol size distribution is

monomodal and the refractive index is wavelength-independent, one has a choice of retrieving the effective radius, the real part of the refractive index, the imaginary part of the refractive index, or the effective variance. The situation becomes even more complicated if the size distribution is bimodal or multimodal and/or if the refractive index varies with wavelength.

For example, Nakajima and Higurashi[19] used a modified power law size distribution and retrieved as the second aerosol parameter the power exponent assuming that the aerosol refractive index is fixed. Higurashi and Nakajima[22] employed a bimodal log normal volume distribution, assumed the same fixed refractive index for both modes, and retrieved the relative contribution of modes 1 and 2 to the total aerosol number density. Obviously, other algorithms are possible.[16] It is thus clear that the performance of several candidate two-channel algorithms must be examined before a "standard" algorithm is selected as the one providing the best *statistical* accuracy.

Another major issue is cloud screening. Even a small cloud contamination of a pixel, if not detected, can lead to a gross overestimation of the retrieved aerosol optical thickness. Several algorithms using different AVHRR spectral channels have been proposed (e.g., Refs. 22–25). However, only the International Satellite Cloud Climatology Project (ISCCP) algorithm has been thoroughly validated,[26] and even this algorithm may need to be modified because it was primarily designed as a conservative *cloud detection* algorithm (most pixels for which the presence of a cloud is in doubt are declared cloud-free), whereas aerosol retrievals may need a more conservative *cloud screening* algorithm (pixels for which the presence of a cloud is in doubt are declared cloudy).

One of the main objectives of the Global Aerosol Climatology Project (GACP; URL: http://gacp.giss.nasa.gov), established in 1998 as a joint initiative of NASA's Radiation Science Program and Global Energy and Water Cycle Experiment (GEWEX), is to retroactively infer the global distribution of aerosols, their properties, and their seasonal and interannual variations for the full period of available satellite data.[27] This is planned to be accomplished primarily through a systematic application of multichannel aerosol retrieval algorithms to existing satellite data and advanced 3-dimensional aerosol chemistry/transport models (e.g., Tegen *et al.*[3]). In this paper we outline the methodology of interpreting channel 1 and 2 AVHRR radiance data over the oceans

and describe a detailed analysis of the sensitivity of retrieved aerosol parameters to the assumptions made in the retrieval algorithms.

Given the strong spatial and temporal variability of tropospheric aerosols and the obvious limitations of two-channel algorithms, it is unreasonable to expect a high accuracy for each instantaneous retrieval. On the other hand, one may expect that imperfections of an algorithm may be partially compensated for by averaging the retrieved aerosol parameters over a sufficiently long period of time. In other words, although a two-channel algorithm cannot be expected to provide accurate daily retrievals, it may still provide rather accurate monthly, decadal, and annual averages that can be quite useful in climate research. Therefore, the strategy that we adopted for our sensitivity analysis was to work with real AVHRR data rather than with computer-generated, synthetic data and to look at the effect of various *a priori* assumptions made in specific candidate algorithms on monthly averages of the retrieved aerosol parameters.

Another feature of our approach is the use of accurate numerical techniques for computing single and multiple scattering and spectral absorption of light in the vertically inhomogeneous atmosphere-ocean system. Two-channel satellite aerosol retrievals represent a complex underdetermined problem and make unavoidable many *a priori* assumptions regarding the parameters of the atmosphere-ocean model. Furthermore, the potentially strong contamination of AVHRR channel 2 radiances by water vapor absorption requires a special treatment. Therefore, the use of accurate numerical methods enabled us to focus on analyzing the effect of inherent uncertainty in model parameters rather than on an examination of possible retrieval artifacts resulting from the use of approximate solution approaches.

2. Satellite Data, Atmosphere-Ocean Model, and Radiative Transfer Code

Our initial activity has focussed on applying several aerosol retrieval algorithms to AVHRR channel 1 and 2 radiance data over the oceans contained in the gridded ISCCP DX dataset. The main advantages of using the ISCCP data product[28] are that it is easily available and contains an

elaborate cloud detection algorithm that can be easily modified for the purposes of aerosol retrievals.

As an initial approximation, we assume that aerosol particles are homogeneous spheres and compute their scattering and radiative properties using the standard Lorenz-Mie theory.[9] The following aerosol parameters serve as an input for the single-scattering Mie code: the type of the aerosol size distribution, size distribution parameters, and real and imaginary parts of the refractive index. A single value is specified for each parameter except for the parameter to be retrieved. For the latter, a grid of values covering the expected range of its variation is provided. The output consists of a file containing the Legendre expansion coefficients of the aerosol phase function, the extinction cross section, and the single scattering albedo for the set of wavelengths used by the multiple-scattering code.

Theoretical channel 1 and 2 reflectances are calculated using a multiple-scattering code based on the scalar version of the adding/doubling method.[9] The code takes into account the rough ocean surface reflection via the modified Kirchhoff approximation,[11] water vapor, oxygen, and CO_2 absorption via the k-distribution technique,[29] and multiple scattering by stratospheric and tropospheric aerosols and molecules.

The distribution of ocean surface slopes is assumed to be Gaussian,

$$p\left(\frac{\partial z}{\partial x},\frac{\partial z}{\partial y}\right)=\frac{1}{2\pi s^2}\exp\left(-\frac{(\partial z/\partial x)^2+(\partial z/\partial y)^2}{2s^2}\right), \tag{1}$$

where the mean square surface slope s^2 is related to the near-surface wind speed W (m/s) via the empirical formula[30]

$$2s^2=0.003+0.00512W. \tag{2}$$

The respective FORTRAN code[11] computes the Fourier components of the ocean bidirectional reflection function using the same grid of Gauss quadrature nodes representing the cosines of the angles of incidence and reflection as the adding/doubling routine. The number of Fourier components must be greater than or equal to the number of Fourier components used in the adding/doubling calculations for the atmosphere. Reflection geometries within 40° off the sun-

glint direction are excluded from the analysis. The upwelling radiances from the ocean body and foam scattering are either ignored or modeled by adding a small Lambertian component to the surface bidirectional reflection function.

The gases that have lines in the first and second AVHRR channels are H_2O, CO_2, and O_2, of which only H_2O and O_2 are significant contributors, although CO_2 is included for the sake of completeness. The gaseous continua that are included are the ozone Chappuis band and the water vapor continuum.[31] The atmospheric temperature and humidity profiles are taken from the ISCCP version of the Television and Infrared Observation Satellite (TIROS) Operational Vertical Sounder (TOVS) data. The total atmosphere is subdivided into a number of homogeneous layers which is increased until convergent results are obtained. In most cases a ten-layer model provides quite sufficient accuracy. The vertical distribution of ozone and water vapor is based on a standard atmospheric profile.[32] Variations in ozone and water vapor are dealt with by scaling the total column amounts appropriately while maintaining the same normalized profile. The vertical profile of the aerosol number density is taken to be the same as the normalized profile of water vapor. Differences between this assumed profile and the actual profiles of water vapor and aerosol are not generally a significant error source in the radiative transfer modeling. There will be some errors in the retrieved aerosol size and optical depth when the majority of the aerosol is above the majority of the water vapor, or when the majority of the aerosol is below the majority of the water vapor. The chosen profile of aerosols provides a balance between these two extremes. Stratospheric aerosols are treated separately using aerosol size, optical depth and vertical profile information from Stratospheric Aerosol and Gas Experiment (SAGE) III.[33]

The radiative transfer code described above can be used to compute a look-up table for any candidate aerosol retrieval algorithm. Each look-up table is a file in which multidimensional arrays of theoretical channel 1 and 2 reflectance values for all viewing geometries and aerosol and atmospheric parameters are stored. The overall dimension of the table is determined by the product of the following parameters:

- relative satellite-sun azimuth angle grid size;

- viewing zenith angle grid size;
- solar zenith angle grid size;
- ozone amount grid size (applies only to the channel 1 part of the look-up table);
- water vapor amount grid size (applies only to the channel 2 part of the look-up table);
- aerosol optical thickness grid size;
- second retrieved aerosol parameter grid size.

The look-up tables are used to retrieve the aerosol optical thickness and a second aerosol parameter using cloud-screened channel 1 and 2 radiance data. The retrieval routine performs a two dimensional search of the minimum of the respective error function using the so-called direction set method,[34] which does not require the calculation of derivatives. The error function is defined as

$$\sqrt{\frac{(L_{1t}-L_{1m})^2+(L_{2t}-L_{2m})^2}{L_{1m}^2+L_{2m}^2}}, \tag{3}$$

where the subscripts 1 and 2 label scaled radiances in the first and second AVHRR channels and the letters *t* and *m* label theoretical and measured quantities, respectively. Iterations continue until the error function becomes smaller than a certain threshold value. Each pixel is mapped on a $1^\circ \times 1^\circ$ global grid. The retrieved values for all pixels within one grid cell are averaged to produce a map for a specified period of time.

It is well known that multidimensional minimization may be a very complicated process and often may result in finding a local rather than a global minimum. Therefore, we have analyzed many particular cases "by hand" and made sure than in all cases considered the minimum found was the global minimum within the specified range of variability of model parameters. Furthermore, in addition to the direction set method, we have also implemented the so-called downhill simplex method.[34] The excellent agreement between the numbers obtained with the two quite independent minimization procedures may also indicate that our retrieval scheme produces reliable results.

3. Sensitivity Analysis

A. Benchmark Atmosphere-Ocean Model

Because the number of candidate algorithms is, in principle, unlimited, we decided to make the scope of our sensitivity analysis manageable by adopting the simple approach of selecting a benchmark atmosphere-ocean model and then examining the changes in the retrieved aerosol parameters caused by variations in adopted model parameters. As the benchmark atmosphere-ocean model, we selected the one based on a modified power law size distribution of the form

$$n(r)=\begin{cases} C, & r\le r_1, \\ C\left(\dfrac{r}{r_1}\right)^{-\alpha}, & r_1<r\le r_2, \\ 0, & r>r_2, \end{cases} \tag{4}$$

with $r_1=0.1\mu\text{m}$, $r_2=10\mu\text{m}$, and $\alpha\in[2.5,5]$. The constant C is uniquely determined from the standard normalization

$$\int_0^\infty \mathrm{d}r\, n(r)=1. \tag{5}$$

Note that larger values of the power exponent α correspond to smaller aerosols and vice versa. The refractive index is assumed to be wavelength-independent and equal to $1.5 + 0.005i$.

Figure 1 shows the respective phase function versus scattering angle and power exponent α. A prominent phase function feature is a significant deepening of the valley at side scattering angles with decreasing α caused by the increasing effect of absorption inside larger aerosols. Figure 2 plots effective radius r_{eff} versus α, where[9]

$$r_{\text{eff}}=\frac{\int_0^\infty \mathrm{d}r\,r\pi r^2 n(r)}{\int_0^\infty \mathrm{d}r\,\pi r^2 n(r)}. \tag{6}$$

Figures 3 and 4 show the Ångström exponent A as a function of α and r_{eff}, respectively, where

$$A = \left.\frac{d[\ln C_{ext}(\lambda)]}{d(\ln\lambda)}\right|_{\lambda=\lambda_1} . \qquad (7)$$

Finally, Fig. 5 shows the power exponent dependence of the single scattering albedo ϖ. ϖ remains nearly constant for $\alpha \geq 4$, but significantly decreases for smaller α due to increasing absorption inside larger aerosol particles.

The contribution of the upwelling radiation from the ocean body and foam scattering is ignored and the wind speed is fixed at a globally uniform value of $W = 7$ m/s.[35]

B. Cloud Screening

Panels (a) and (b) of Fig. 6 show monthly mean optical thickness $<\tau>$ and optical-thickness-weighted power exponent $<\alpha>$ for July of 1986 retrieved using the standard ISCCP cloud detection scheme,[24] the ISCCP calibration of the first AVHRR channel,[28] and the pre-launch calibration of the second channel. The ISCCP cloud detection scheme includes the following five major steps: (1) applying a space contrast test to individual infrared (IR) images; (2) applying a time contrast test to three consecutive IR images at constant diurnal phase; (3) cumulation of space/time statistics using both IR and visible images; (4) construction of composite clear-sky visible radiances and IR temperatures once every 5 days at each diurnal phase and location; and (5) applying radiance and temperature thresholds by comparing measured radiances and IR temperatures to the respective composite values.

The relatively large optical thickness values in Fig. 6(a) may indicate a significant residual cloud contamination of many pixels that were classified as clear sky and suggest that the standard ISCCP criteria for detecting clear sky pixels may need to be tightened. It is well known that the effect of aerosols and clouds on visible channel reflectances is similar, whereas AVHRR channel 5 ($\lambda_5 = 11.7\mu$m) reflectances are not affected by aerosols because of their negligibly small optical thickness at infrared wavelengths. Therefore, it is likely that tightening the visible ISCCP threshold or imposing an additional visible radiance threshold rejecting pixels with channel 1 or channel 2 radiances exceeding a certain value may result in an adverse loss of pixels with

significant aerosol loads. On the other hand, tightening the IR threshold can be expected to mostly affect only the results of cloud detection. Panels (c) and (d) of Fig. 6 present the retrieval results obtained with a modified ISCCP cloud screening scheme which retains only pixels with IR temperatures warmer than the composite values. Contrasting Figs. 6(a) and 6(c) shows a significant overall decrease in $<\tau>$, but a relatively weak effect on the pixels with large values of the optical thickness. Another noticeable effect is a significant overall increase in the mean power exponent and, thus, a decrease in the average particle size. Both effects are consistent with the assumption that the more conservative cloud screening algorithm removes more cloud-contaminated pixels and the fact that typical cloud particles are larger than typical aerosols. The results of Refs. 36–38 may indicate that the types of clouds eliminated by this algorithm are small cumulus clouds and optically thin cirrus.

Panels (a) and (b) of Fig. 7 show the results obtained with an even more conservative cloud screening scheme, which retains only pixels warmer than the respective composite temperatures by 1K or more. It is obvious that the overall $<\tau>$ is further decreased, whereas the cases of large aerosol loads are hardly affected. The effect on $<\alpha>$ is weaker and less obvious. Large $<\alpha>$ seem to further slightly increase and small $<\alpha>$ seem to slightly decrease, but this may be an artifact of reducing statistics (see below).

Wagener *et al.*[25] suggested to use the channel 1 to channel 2 radiance ratio, S_{12}, as an additional indicator of cloud contamination by rejecting all pixels with $S_{12}<1.5$ or $S_{12}>3.5$. This criterion is based on the observations that $S_{12} \leq 1$ for totally overcast pixels or data over land surfaces. Panels (c) and (d) of Fig. 7 show the results obtained by superimposing the S_{12} criterion on the more conservative IR threshold used for Figs. 7(a) and 7(b). The overall change is relatively small, although some spurious cases of large τ at high northern and southern latitudes are removed.

The results of the above sensitivity tests clearly demonstrate that accurate cloud screening is an issue of critical importance. Applying increasingly conservative thresholds may further reduce the risk of cloud contamination, but also reduces the amount of useful aerosol data [as already

manifested by the increased number of white pixels in Fig. 7(c) as compared to Fig. 6(a)] and may ultimately introduce a significant statistical bias. For example, the latter three cloud screening schemes rejected, respectively, 56.5%, 78.8%, and 79.9% of the pixels originally classified by ISCCP as cloud-free. The latter two numbers are consistent with the estimate of the amount of clouds missing by ISCCP derived by Liao *et al.*[37] from SAGE II data. Therefore, we decided to adopt for the following analysis the combination of the conservative IR scheme (retaining only pixels warmer than the composite values by 1K or more) and the $1.5 < S_{12} < 3.5$ criterion. It is obvious, however, that the definitive examination of the quality of the product generated by this algorithm will require extensive comparisons with long-term ground-based measurements and, possibly, future results from more advanced satellite instruments.[39]

The most obvious features of the optical thickness patterns in Fig. 7(c) are the plumes of African and Asian dust and aerosols produced by biomass burning in Equatorial Africa and South America. Dust aerosols can also be clearly identified in the power exponent map [Fig. 7(d)] due to their larger sizes. Figure 7(d) shows a remarkable asymmetry in the average aerosol size: the northern hemisphere seems to be dominated by relatively small particles, presumably anthropogenic pollutants, whereas a large fraction of the southern hemisphere is covered by significantly larger particles, most likely sea salt aerosols. Figure 8 depicts the global average as well as the northern and southern hemisphere averages of the aerosol optical thickness and optical-thickness-weighted power exponent retrieved over the full period of *NOAA-9* observations. The aerosols in the southern hemisphere indeed appear to be systematically larger as well as optically thinner than those in the northern hemisphere.

C. Effect of Radiance Calibration Uncertainties

The retrievals described in the previous section were based on the ISCCP post-launch calibration of the *NOAA-9* AVHRR channel 1 and the pre-launch calibration of channel 2. It is known that the in-flight degradation of channel 2 was significantly slower than that of channel 1.[40] This may explain why neither curve in Fig. 8 shows a significant long-term trend. There may be a slight

overall increase in the power law exponent, which would be consistent with the fact that the in-flight degradation of channel 1 was and that of channel 2 was not corrected for, thereby increasing the spectral contrast between the channels and reducing the retrieved particle size. However, even if this trend is real, it is very weak.

The post-launch calibration of AVHRR channels 1 and 2 is a very complicated problem associated with many uncertainties and discrepancies.[40,41] To examine the potential effect of calibration uncertainties on the two-channel aerosol retrievals, we have recomputed Figs. 7(a) and 7(b) using the NOAA post-launch calibration of both visible channels.[40] Comparison of Figs. 7(a) and 7(b) with Figs. 9(a) and 9(b), respectively, shows significant changes in both the optical thickness and the power law exponent patterns, especially in the regions with small aerosol loads. We have found that these changes are mainly caused by very small differences in the assumed values of the so-called deep space count (the response of the radiometer to zero incident intensity) between the ISCCP and NOAA calibrations of channel 1 and the pre-launch and NOAA post-launch calibrations of channel 2. Although these differences cause percent scaled radiance differences as small as a few tenths of a percent, the effect on the accuracy of retrieving small optical thickness values is rather strong. Because aerosol retrievals over the ocean surface deal with small measured radiances and because the aerosol contribution to the total radiance is often weak, we have to conclude that the post-launch calibration issue for channels 1 and 2 may need to be revisited before one attempts a massive aerosol retrieval for the full period of available AVHRR data.

There is no doubt that the two-channel AVHRR retrievals will be very useful for studying monthly and seasonal variability of spatial patterns of aerosol parameters. However, the very methodology that has to be used for the post-launch calibration[40,41] and its rather poor accuracy make it difficult to expect that these retrievals by themselves can detect a slow trend in the aerosol optical thickness and/or size with accuracy needed for climate change studies.[5] Our results demonstrate once again that reliable detection of a long-term trend in climatically important aerosol parameters may require the use of a much more accurate remote-sensing technique such as high-precision polarimetry.[11,12,15]

D. Different Ways of Averaging the Power Exponent

Figure 7(d) shows the optical-thickness-weighted monthly mean power law exponent computed as

$$<\alpha>=\frac{1}{T<\tau>}\int_{t}^{t+T}\alpha(t)\tau(t)\,dt, \tag{8}$$

where

$$<\tau>=\frac{1}{T}\int_{t}^{t+T}\tau(t)\,dt. \tag{9}$$

This quantity is a measure of the average size of aerosols suspended in the atmosphere at a given location during the month. An alternative definition is

$$\overline{\alpha}=\frac{1}{T}\int_{t}^{t+T}\alpha(t)\,dt \tag{10}$$

and indicates the aerosol size encountered most frequently during the same period of time without indicating how much aerosol had that size. $<\alpha>$ may differ significantly from $\overline{\alpha}$ if there is a strong correlation between α and τ, but should be nearly the same if the correlation is absent or weak.

Figure 9(c) shows a map of $\overline{\alpha}$ for July of 1986 and should be contrasted to Fig. 7(d), whereas Fig. 9(d) maps the ratio $\overline{\alpha}/<\alpha>$. One sees that in most cases the difference between $\overline{\alpha}$ and $<\alpha>$ is within ±10%, which indicates a weak correlation between α and τ on the global scale. This conclusion is corroborated by Fig. 10, which presents a regression of α against τ and shows no obvious correlation. On the other hand, Fig. 9(d) may indicate the presence of significant local correlations, especially in the southern hemisphere.

E. Effect of Aerosol Absorption

Recent studies have shown that a significant fraction of tropospheric aerosols (especially the mineral dust and biomass burning components) can be rather strongly absorbing.[42–45] This may justify the choice of a nonzero imaginary part of the refractive index for a unified aerosol model

used in global AVHRR retrievals. However, many remote areas can be dominated by nonabsorbing aerosols such as sea salt, and the total single scattering albedo can be significantly closer to unity than is shown by the solid curve in Fig. 5. Panels (a) and (b) of Fig. 11 show the ratios of the average optical thickness and optical-thickness-weighted power exponent retrieved with the same aerosol model but assuming an imaginary part of the refractive index of Im(m) = 0.002 relative to those displayed in Figs. 7(c) and 7(d), respectively. The most obvious result of decreasing absorption is an overall decrease in the retrieved optical thickness. The decrease is especially significant and can exceed 25% in areas dominated by larger aerosols (smaller power exponents) as well as in areas with heavy aerosol loads. These changes can be explained by increased phase function values at side- and back-scattering geometries for larger particles (cf. Figs. 1 and 12) and by systematically larger single scattering albedos (cf. solid and dashed curves in Fig. 5). On the other hand, decreasing absorption does not seem to have a significant effect on the retrieved aerosol size [Fig. 11(b)].

It is thus clear that the use of a globally-unified imaginary part of the refractive index can result in significant systematic regional and/or seasonal errors in the retrieved aerosol optical thickness. Since Im(m) cannot be inferred from AVHRR channel 1 and 2 data, this result may call for applying several aerosol models with different Im(m) values and using auxiliary information such as Total Ozone Mapping Spectrometer (TOMS) data[46] or results of aerosol transport modeling[3] as indicators of the likely magnitude of aerosol absorption. Of course, this would result in a much more complicated and time-consuming retrieval algorithm. Furthermore, absorption can be spectrally dependent, thereby potentially affecting the retrievals of the aerosol size.

F. Effect of the Real Part of the Refractive Index

It is well known that the real part of the aerosol refractive index may be highly variable in space and time and may differ significantly from the adopted benchmark value 1.5.[47] To examine potential retrieval errors caused by this variability, we performed retrievals similar to those shown in panels (c) and (d) of Fig. 7, but assuming a refractive index value of $1.4 + 0.005i$.

Figures 13(a) and 13(b) show the ratios of the aerosol optical thickness and power exponent thus obtained relative to those shown in Figs. 7(c) and 7(d), respectively. The most notable result is a substantial overall increase of the optical thickness and a very little change in the power exponent. The former is obviously caused by systematically lower phase function and single scattering albedo values for Re(m) = 1.4 (cf. Figs. 1, 5, and 14). This test suggests that adopting a fixed, globally uniform refractive index may result in significant instantaneous retrieval errors and, potentially, in a systematic regional and seasonal bias in areas dominated by a single aerosol type with refractive index significantly different from the adopted value. A feasible, but cumbersome solution of this problem could be to constrain the refractive index range by employing auxiliary information provided, e.g., by aerosol transport models.

G. Effect of Diffuse Ocean Reflectance

Previous results were obtained assuming no upwelling radiance contribution caused by scattering beneath the ocean surface and by foam. Depending on meteorological conditions and location, this diffuse contribution can be significant[48–51] but is difficult to parameterize for the purpose of the global aerosol retrieval. Most of existing parameterizations require (often unavailable) information on the real-time wind speed and pigment concentration, were derived under specific natural or even artificial conditions, and may not be readily generalized. One may expect that the use of the previously described S_{12} threshold may eliminate the cases of most significant foam contamination caused by wind speeds exceeding 12 m/s because foam tends to reduce the contrast between channel 1 and 2 radiances. Furthermore, by selecting relatively warmer pixels our algorithm favors the cases with higher ocean surface temperatures and, thus, lower wind speeds. In addition, pixels with very high wind speeds are more likely to be cloudy. For lower wind speeds, one may have to use the simplest parameterization of the diffuse ocean reflectance by adding a small, uniform Lambertian component to the ocean surface reflection function as suggested by Stowe *et al.*[8]

Panels (c) and (d) of Fig. 11 demonstrate the effect of adding a fixed 0.003 Lambertian component that slightly exceeds the 0.002 component used in Ref. 8. The most obvious and natural result is an overall reduction of the optical thickness. This change is especially noticeable in the cases of low aerosol loads, but is within 10% in the majority of other cases. A secondary (and mostly negligible) effect is a slight increase in the retrieved power exponent caused by the implicit increase of the spectral contrast in the aerosol scattering contribution to the total reflectance. The latter effect may further weaken if the foam contribution itself shows a spectral contrast comparable to that of aerosols.[49,50]

H. Effect of Wind Speed

The deviation of the actual wind speed from the benchmark 7 m/s value may also cause retrieval errors via changing the specular component of the ocean reflection function [Eqs. (1) and (2)]. Because the actual real-time value of the wind speed is often unknown and cannot be inferred from AVHRR data, one must examine the potential effect of adopting a globally uniform and constant wind speed value. Panels (c) and (d) of Fig. 13 computed for W = 11 m/s as well as similar computations for wind speed values smaller than 7 m/s (not shown) suggest that the retrieval errors in the optical thickness should be less that 10% in most cases, whereas the errors in the power exponent are negligibly small. Only in cases of very low aerosol loads ($\tau \leq 0.05$) the errors in the retrieved optical thickness can exceed 25%. These results are in a good agreement with those derived by Higurashi and Nakajima.[22] Despite this relatively weak sensitivity, one may expect that making use of advanced global ocean wind speed data sets[52] can further improve the accuracy of satellite aerosol retrievals.

I. Effect of Size Distribution Function

The modified power law used in the benchmark model is not necessarily the best representation of the actual shape of the aerosol size distribution in many cases, and other distribution functions such

as gamma and log normal distributions have often been used. Figure 15 summarizes the retrieval results obtained with a modified bimodal log normal distribution of the form[22]

$$n(r) = C_1 r^{-4}\left[\exp\left(-\frac{(\ln r - \ln r_{g1})^2}{2\ln^2 \sigma_{g1}^2}\right) + \gamma \exp\left(-\frac{(\ln r - \ln r_{g2})^2}{2\ln^2 \sigma_{g2}^2}\right)\right] \tag{11}$$

with $r_{g1} = 0.17\mu m$, $r_{g2} = 3.44\mu m$, $\sigma_{g1} = 1.96$, $\sigma_{g1} = 2.37$, and $\gamma \in [0.1, 100]$ and assuming the benchmark refractive index value $m = 1.5 + 0.005i$. Again, the constant C_1 is determined from the normalization condition of Eq. (5). Figures 16 and 17 show the respective phase function and single scattering albedo.

A very important conclusion following from Fig. 15(a) is that despite the large difference in the functional form of the power law and bimodal size distributions, the respective monthly mean optical thicknesses are remarkably similar and in most cases are within ±10% of each other. The retrieved monthly mean effective radii are in a much worse agreement and may differ by more than a factor of two. This may be explained by a significantly narrower range of possible r_{eff} values for the bimodal size distribution and the saturation of A with increasing r_{eff} for the power law distribution (Fig. 4). As a result, the retrieval algorithm based on the bimodal size distribution tends to produce smaller effective radii than that based on the power law distribution. The differences in the respective optical-thickness-weighted mean Ångström exponents <A> as well as in the simple mean Ångström exponents $\overline{A}$ [cf. Eqs. (8) and (10)] appear to be less significant than those in r_{eff}. In most cases the differences in <A> and $\overline{A}$ do not exceed 0.3 and 0.2, respectively. These results may suggest that $\overline{A}$ is the aerosol size characteristic least sensitive to the uncertainties in the atmosphere-ocean model and should be retrieved along with optical thickness as the second aerosol parameter.

J. Two-Channel Versus One-Channel Aerosol Retrievals

In order to compare the expected performance of two-channel and one-channel retrieval algorithms, we repeated retrievals using the benchmark aerosol model with five fixed power

exponent values (α=2.5, 3, 3.5, 4, and 4.5), utilizing only AVHRR channel-1 radiance data, and retrieving only the aerosol optical thickness. The results of this test are summarized in Figs. 18 and 19, which show a remarkable zonal structure most likely caused by seasonality of predominant AVHRR scattering geometries and systematic phase function differences for different values of α (Fig. 1). The differences in the retrieved optical thickness for different fixed α can exceed 300% and are indicative of biases that can be expected if a one-channel algorithm employs a fixed aerosol size not representative of the seasonally and/or regionally dominant aerosol type. As a whole, contrasting Fig. 15(a) with Figs. 18 and 19 convincingly demonstrates the great advantage of utilizing AVHRR channel 2 data in addition to channel 1 radiances.

4. Conclusions

The main results of our sensitivity study of the expected performance of two-channel aerosol retrieval algorithms based on real AVHRR data can be summarized as follows.

- Two-channel algorithms can be expected to provide significantly more accurate and less biased retrievals of the aerosol optical thickness than one-channel algorithms.

- Imperfect cloud screening and calibration uncertainties are by far the largest sources of errors in the retrieved optical thickness. Both problems are difficult to solve definitively and should be addressed by means of extensive ground-based observations, careful statistical analyses of the radiance data, and, potentially, comparisons with future results from more advanced satellite instruments.

- Two different ways of computing the average aerosol size (direct versus optical-thickness-weighted) can be expected to produce similar results because of weak correlation between the aerosol optical thickness and size.

- Both underestimating and overestimating aerosol absorption as well as the potentially strong variability of the real part of the aerosol refractive index may lead to regional and/or seasonal biases in the retrieved aerosol optical thickness.

- Deviations of the actual wind speed from the global mean value 7 m/s within the range from 0 to 11 m/s have little effect on the retrieved optical thickness. Neglecting the diffuse component of the ocean reflection function can affect the retrieved optical thickness in the cases of low aerosol loads.

- Simple monthly average of the Ångström exponent appears to be the most invariant aerosol size characteristic and should be retrieved along with optical thickness as the second aerosol parameter.

It may be expected that the two-channel retrieval algorithms could be improved by adopting time-dependent regional aerosol models. For example, dust particles have distinctly nonspherical shapes and their scattering properties can differ substantially from those for surface- or volume-equivalent spheres.[53–57] It is feasible, therefore, that using a nonspherical aerosol model can improve the accuracy of optical thickness retrievals over areas where dust aerosols are the dominant component.[58] In addition, TOMS data could be used to determine areas with predominantly absorbing aerosols.[46]

Although our analysis demonstrates the expected range of retrieval errors caused by unavoidable uncertainties in the assumed parameters of the atmosphere-ocean model, it cannot determine the best choice of fixed, globally uniform values for all model parameters other than two parameters that are being retrieved. This choice can only be made on the basis of an extensive validation versus statistically representative ground-based and in situ measurements. This work has already begun (e.g., Refs. 22 and 59) and will be an important part of the GACP. Another aspect of sensitivity studies that needs to be addressed is the analysis of the effect of radiance calibration and water vapor amount errors on the retrieved aerosol parameters. It is expected that candidate retrieval algorithms will be further refined by using retrievals from POLDER[59] and

results from future space missions[39] and then re-applied to the full AVHRR data set. We also plan to use future airborne results from the Research Scanning Polarimeter built by SpecTIR Corporation.[60]

We thank two anonymous reviewers for useful comments on an earlier version of this paper and Nadia Zakharova for help with color graphics. This research was sponsored by the NASA Radiation Science Program managed by Robert Curran.

References

1. *Intergovernmental Panel on Climate Change, Climate Change 1995* (Cambridge Univ. Press, New York, 1995).
2. E. Roeckner, T. Siebert, and J. Feichter, "Climatic response to anthropogenic sulfate forcing simulated with a general circulation model," in *Aerosol Forcing of Climate*, R. Charlson and J. Heintzenberg, eds. (Wiley, New York, 1995), pp. 349–362.
3. I. Tegen, P. Hollrigl, M. Chin, I. Fung, D. Jacob, and J. Penner, "Contribution of different aerosol species to the global aerosol extinction optical thickness: Estimates from model results," J. Geophys. Res. **102**, 23,895–23,915 (1997).
4. R. L. Miller and I. Tegen, Radiative forcing of a tropical direct circulation by soil dust aerosols," J. Atmos. Sci. **56**, 2403–2433 (1999).
5. J. Hansen, M. Sato, R. Ruedy, A. Lacis, *et al.*, "Forcings and chaos in interannual to decadal climate change," J. Geophys. Res. **102**, 25,679–25,720 (1997).
6. A. A. Lacis and M. I. Mishchenko, "Climate forcing, climate sensitivity, and climate response: A radiative modeling perspective on atmospheric aerosols," in *Aerosol Forcing of Climate*, R. Charlson and J. Heintzenberg, eds. (Wiley, New York, 1995), pp. 11–42.
7. O. B. Toon, "Modeling the relationships between aerosol properties and the direct and indirect effects of aerosols on climate," in *Aerosol Forcing of Climate*, R. Charlson and J. Heintzenberg, eds. (Wiley, New York, 1995), pp. 197–213.
8. L. L. Stowe, A. M. Ignatov, and R. R. Singh, "Development, validation, and potential enhancements to the second-generation operational aerosol product at the National Environmental Satellite, Data, and Information Service of the National Oceanic and Atmospheric Administration," J. Geophys. Res. **102**, 16,923–16,934 (1997).
9. J. E. Hansen and L. D. Travis, "Light scattering in planetary atmospheres," Space Sci. Rev. **16**, 527–610 (1974).
10. M. Wang and H. R. Gordon, "Estimating aerosol optical properties over the oceans with the multiangle imaging spectroradiometer: Some preliminary results," Appl. Opt. **33**, 4042–4057 (1974).

11. M. I. Mishchenko and L. D. Travis, "Satellite retrieval of aerosol properties over the ocean using polarization as well as intensity of reflected sunlight," J. Geophys. Res. **102**, 16,989–17,013 (1997).

12. M. I. Mishchenko and L. D. Travis, "Satellite retrieval of aerosol properties over the ocean using measurements of reflected sunlight: Effect of instrumental errors and aerosol absorption," J. Geophys. Res. **102**, 13,543–13,553 (1997).

13. A. Ignatov, L. Stowe, and R. Singh, "Validation of the NOAA/NESDIS operational aerosol retrievals using TARFOX data," EOS Trans. AGU **78**, Spring Meet. Suppl., S87 (1997).

14. S. Twomey, "Pollution and the planetary albedo," Atmos. Environ. **8**, 1251–1256 (1974).

15. M. I. Mishchenko, L. D. Travis, W. B. Rossow, B. Cairns, B. E. Carlson, and Q. Han, "Retrieving CCN column density from single-channel measurements of reflected sunlight over the ocean: A sensitivity study," Geophys. Res. Lett. **24**, 2655–2658 (1997).

16. P. Durkee, F. Pfeil, E. Frost, and E. Shima, "Global analysis of aerosol particle characteristics," Atmos. Environ. A **25**, 2457–2471 (1991).

17. D. Tanré, Y. J. Kaufman, M. Herman, and S. Mattoo, "Remote sensing of aerosol properties over oceans using the MODIS/EOS spectral radiances," J. Geophys. Res. **102**, 16,971–16,988 (1997).

18. T. Nakajima and A. Higurashi, "A use of two-channel radiances for an aerosol characterization from space," Geophys. Res. Lett. **25**, 3815–3818 (1998).

19. T. Nakajima, and A. Higurashi, "AVHRR remote sensing of aerosol optical properties in the Persian Gulf region, summer 1991," J. Geophys. Res. **102**, 16,935–19,946 (1997).

20. D. Tanré, Y. J. Kaufman, M. Herman, and S. Mattoo, "Remote sensing of aerosol properties over oceans using the MODIS/EOS spectral radiances," J. Geophys. Res. **102**, 16,971–16,988 (1977).

21. R. Kahn, P. Banerjee, D. McDonald, and D. J. Diner, "Sensitivity of multiangle imaging to aerosol optical depth and to pure-particle size distribution and composition over ocean," J. Geophys. Res. **103**, 32,195–32,213 (1998).

22. A. Higurashi and T. Nakajima, "Development of a two channel aerosol retrieval algorithm on global scale using NOAA/AVHRR," J. Atmos. Sci. **56**, 924–941 (1999).

23. E. P. McClain, "Global sea surface temperatures and cloud clearing for aerosol optical depth estimates," Int. J. Remote Sens. **10**, 763–769 (1989).

24. W. B. Rossow and L. C. Garder, "Cloud detection using satellite measurements of infrared and visible radiances for ISCCP," J. Clim. **6**, 2341–2369 (1993).

25. R. Wagener, S. Nemesure, and S. E. Schwartz, "Aerosol optical depth over oceans: High space- and time-resolution retrieval and error budget from satellite radiometry," J. Atmos. Oceanic Technol. **14**, 577–590 (1997).

26. W. B. Rossow and L. C. Garder, "Validation of ISCCP cloud detection," J. Clim. **6**, 2370–2393 (1993).

27. R. Curran, M. Mishchenko, I. Tegen, and I. Geogdzhayev, "Global Aerosol Climatology Project (GACP): Structure, early products and plans," GEWEX News **8**(4), 3–4 (1998).

28. W. B. Rossow, A. W. Walker, D. E. Beuschel, and M. D. Roiter, "International Satellite Cloud Climatology Project (ISCCP) Documentation of New Cloud Data Sets," World Climate Research Programme, Geneva, Switzerland, WMO/TD-No. 737 (1996).

29. A. A. Lacis and V. Oinas, "A description of the correlated k-distribution method for modeling non-grey gaseous absorption, thermal emission, and multiple scattering in vertically inhomogeneous atmospheres," J. Geophys. Res. **96**, 9027–9063 (1991).

30. C. Cox and W. Munk, "Statistics of the sea surface derived from Sun glitter," J. Marine Res. **13**, 198–227 (1954).

31. R. H. Tipping and Q. Ma, "Theory of the water vapor continuum and validations," Atmos. Res. **36**, 69–94 (1995).

32. R. A. McClatchey, R. W. Fenn, J. E. A. Selby, F. E. Volz, and J. S. Garing, "Optical properties of the atmosphere," Environ. Res. Paper 411, Air Force Cambridge Research Laboratory, Bedford, Mass. (1972).

33. A. A. Lacis, B. E. Carlson, and J. E. Hansen, "Retrieval of atmospheric NO_2, O_3, aerosol optical depth, effective radius and variance information from SAGE II multi-spectral extinction measurements," Appl. Math. Comput., in press (1999).

34. W. H. Press, S. A. Teukolsky, W. T. Vetterling, and B. P. Flannery, *Numerical Recipes in FORTRAN* (Cambridge Univ. Press, Cambridge, 1992).

35. J. Hsiung, "Mean surface energy fluxes over the global ocean," J. Geophys. Res. **91**, 10,585–10,606 (1986).

36. B. A. Wielicki and L. Parker, "On the determination of cloud cover from satellite sensors: the effect of sensor spatial resolution," J. Geophys. Res. **97**, 12,799–12,823 (1992).

37. X. Liao, W. B. Rossow, and D. Rind, "Comparison between SAGE II and ISCCP high-level clouds. 1. Global and zonal mean cloud amounts," J. Geophys. Res. **100**, 1121–1135 (1995).

38. T. C. Benner and J. A. Curry, "Characteristics of small tropical cumulus clouds and their impact on the environment," J. Geophys. Res. **103**, 28,753–28,767 (1998).

39. G. Asrar and R. Greenstone (Eds.), "1995 MTPE EOS Reference Handbook" (National Aeronautics and Space Administration, Washington, DC, 1995).

40. C. R. N. Rao (Ed.), "Degradation of the visible and near-infrared channels of the Advanced Very High Resolution Radiometer on the NOAA-9 spacecraft: assessment and recommendations for corrections," NOAA Tech. Rep. NESDIS 70, National Oceanic and Atmospheric Administration, Washington, DC (1993).

41. C. L. Brest, W. B. Rossow, M. D. Roiter, "Update of radiance calibrations for ISCCP," J. Atmos. Ocean. Technol. **14**, 1091–1109 (1997).

42. I. Sokolik, A. Andronova, and T. C. Johnson, "Complex refractive index of atmospheric dust aerosols," Atmos. Environ. A **27**, 2495–2502 (1993).

43. P. V. Hobbs, J. S. Reid, R. A. Kotchenruther, R. J. Ferek, and R. Weiss, "Direct radiative forcing by smoke from biomass burning," Science **275**, 1776–1778 (1997).

44. D. A. Hegg, J. Livingston, P. V. Hobbs, T. Novakov, and P. Russell, "Chemical apportionment of aerosol column optical depth off the mid-Atlantic coast of the United States," J. Geophys. Res. **102**, 25,293–25,303 (1997).

45. O. Dubovik, B. N. Holben, Y. J. Kaufman, M. Yamasoe, A. Smirnov, D. Tanré, and I. Slutsker, "Single-scattering albedo of smoke retrieved from the sky radiance and solar transmittance measured from ground," J. Geophys. Res. **103**, 31,903–31,923 (1998).

46. O. Torres, P. K. Bhartia, J. R. Herman, Z. Ahmad, and J. Gleason, "Derivation of aerosol properties from satellite measurements of backscattered ultraviolet radiation: Theoretical basis," J. Geophys. Res. **103**, 17,099–17,110 (1998).

47. G. A. d'Almeida, P. Koepke, and E. P. Shettle, *Atmospheric Aerosols* (A. Deepak Publishing, Hampton, Va., 1991).

48. P. Koepke, "Effective reflectance of oceanic whitecaps," Appl. Opt. **23**, 1816–1824 (1984).

49. R. Frouin, M. Schwindling, and P.-Y. Deschamps, "Spectral reflectance of sea foam in the visible and near-infrared: In situ measurements and remote sensing implications," J. Geophys. Res. **101**, 14,361–14,371 (1996).

50. K. D. Moore, K. J. Voss, and H. R. Gordon, "Spectral reflectance of whitecaps: Instrumentation, calibration, and performance in coastal waters," J. Atmos. Oceanic Technol. **15**, 496–509 (1998).

51. H. R. Gordon, O. B. Brown, R. H. Evans, J. W. Brown, R. C. Smith, K. S. Baker, and D. K. Clark, "A semianalytic radiance model of ocean color," J. Geophys. Res. **93**, 10,909–10,924 (1988).

52. I. R. Young, "Seasonal variability of the global ocean wind and wave climate," Int. J. Climatol. **19**, 931–950 (1999).

53. T. Nakajima, M. Tanaka, M. Yamano, M., *et al.*, "Aerosol optical characteristics in the yellow sand events observed in May, 1982 at Nagasaki. II: Models," J. Meteorol. Soc. Japan **67**, 279–291 (1989).

54. M. I. Mishchenko, M. I., L. D. Travis, R. A. Kahn, and R. A. West, "Modeling phase functions for dustlike tropospheric aerosols using a shape mixture of randomly oriented polydisperse spheroids," J. Geophys. Res. **102**, 16,831–16,847 (1997).

55. N. A. Krotkov, D. E. Flittner, A. J. Krueger, A. Kostinski, C. Riley, W. Rose, and O. Torres, "Effect of particle non-sphericity on satellite monitoring of drifting volcanic ash clouds," J. Quant. Spectrosc. Radiat. Transfer **63**, 613–630 (1999).

56. Y. Liu, W. P. Arnott, and J. Hallett, "Particle size distribution from multispectral optical depth: Influences of particle nonsphericity and refractive index," J. Geophys. Res., in press (1999).

57. P. Yang and K. N. Liou, "Finite difference time domain method for light scattering by nonspherical and inhomogeneous particles," in *Light Scattering by Nonspherical Particles: Theory, Measurements, and Applications*, M. I. Mishchenko, J. W. Hovenier, and L. D. Travis, eds. (Academic Press, 1999), pp. 173–221.

58. M. I. Mishchenko, A. A. Lacis, B. E. Carlson, and L. D. Travis, "Nonsphericity of dust-like tropospheric aerosols: implications for aerosol remote sensing and climate modeling," Geophys. Res. Lett. **22**, 1077–1080 (1995).

59. P. Goloub, D. Tanré, J. L. Deusé, M. Herman, A. Marchand, and F.-M. Bréon, "Validation of the first algorithm applied for deriving the aerosol properties over the ocean using the POLDER/ADEOS measurements," IEEE Trans. Geosci. Remote Sens. **37**, 1586–1596 (1999).

60. B. Cairns, L. D. Travis, and E. E. Russell, "The Research Scanning Polarimeter: calibration and ground-based measurements," Proc. SPIE **3754**, in press (1999) (URL: http://www.giss.nasa.gov/data/rsp_air/rspmain.html).

Figure captions

Fig. 1. Phase function versus power exponent and scattering angle for the power law size distribution of Eq. (4) and $m = 1.5 + 0.005i$.

Fig. 2. Effective radius versus power exponent for the power law size distribution of Eq. (4).

Fig. 3. Ångström exponent versus power exponent for the power law size distribution of Eq. (4).

Fig. 4. Ångström exponent versus effective radius for the power law size distribution of Eq. (4) and the bimodal size distribution of Eq. (11).

Fig. 5. Single scattering albedo versus power exponent for the power law size distribution of Eq. (4) and three values of the refractive index.

Fig. 6. (a) and (b): Monthly mean optical thickness $< \tau >$ and optical-thickness-weighted power exponent $< \alpha >$ for July of 1986 derived using the benchmark atmosphere-ocean model and the standard ISCCP cloud detection scheme. (c) and (d): As in panels (a) and (b), but using a modified cloud detection scheme that retains only pixels with channel 5 temperatures warmer than the respective composite values.

Fig. 7. (a) and (b): As in panels (a) and (b) of Fig. 6, but using the cloud detection scheme that retains only pixels with channel 5 temperatures warmer than their composite counterparts by 1K or more. (c) and (d): As in panels (a) and (b), but with the addition of the S_{12} threshold.

Fig. 8. Global and hemisphere averages of the aerosol optical thickness and power exponent plotted with daily resolution. The horizontal ticks correspond to the 15th day of the respective months.

Fig. 9. (a) and (b): As in panels (a) and (b) of Fig. 7, but using the NOAA post-launch calibration of *NOAA-9* AVHRR channels 1 and 2. (c): As in panel (d) of Fig. 7, but for $\overline{\alpha}$. (d): The $\overline{\alpha} / < \alpha >$ ratio.

Fig. 10. Scatterplot of aerosol power exponent versus optical thickness for July of 1986.

Fig. 11. (a) and (b): Ratios of the mean optical thickness and power exponent retrieved assuming the refractive index $m = 1.5 + 0.002i$ relative to those shown in Figs. 7(c) and 7(d), respectively. (c) and (d): Ratios of the mean optical thickness and power exponent retrieved assuming a small added diffuse contribution to the ocean reflection function relative to those shown in Figs. 7(c) and 7(d), respectively.

Fig. 12. Phase function versus power exponent and scattering angle for the power law size distribution of Eq. (4) and $m = 1.5 + 0.002i$.

Fig. 13. (a) and (b): Ratios of the mean optical thickness and power exponent retrieved assuming the refractive index $m = 1.4 + 0.005i$ relative to those shown in Figs. 7(c) and 7(d), respectively. (c) and (d): Ratios of the mean optical thickness and power exponent retrieved assuming a wind speed of $W = 11$ m/s relative to those shown in Figs. 7(c) and 7(d), respectively.

Fig. 14. Phase function versus power exponent and scattering angle for the power law size distribution of Eq. (4) and $m = 1.4 + 0.005i$.

Fig. 15. (a): Ratio of monthly mean aerosol optical thicknesses retrieved using the bimodal size distribution of Eq. (11) and the modified power law of equation (4). (b): As in (a), but for the effective radius ratio. (c): As in (a), but for the difference of optical-thickness-weighted monthly mean Ångström exponents. (d): As in (c), but for the difference of simple monthly mean Ångström exponents.

Fig. 16. Phase function versus γ and scattering angle for the bimodal log normal size distribution of Eq. (11) and $m = 1.5 + 0.005i$.

Fig. 17. Single scattering albedo versus γ for the bimodal log normal size distribution of Eq. (11) and $m = 1.5 + 0.005i$.

Fig. 18. Aerosol optical thickness retrieved with the one-channel algorithm based on the power law size distribution of Eq. (4) with $\alpha = 2.5$, 3, 4, and 4.5 relative to that retrieved for $\alpha = 3.5$ for July of 1986.

Fig. 19. As in Fig. 18, but for January of 1986.

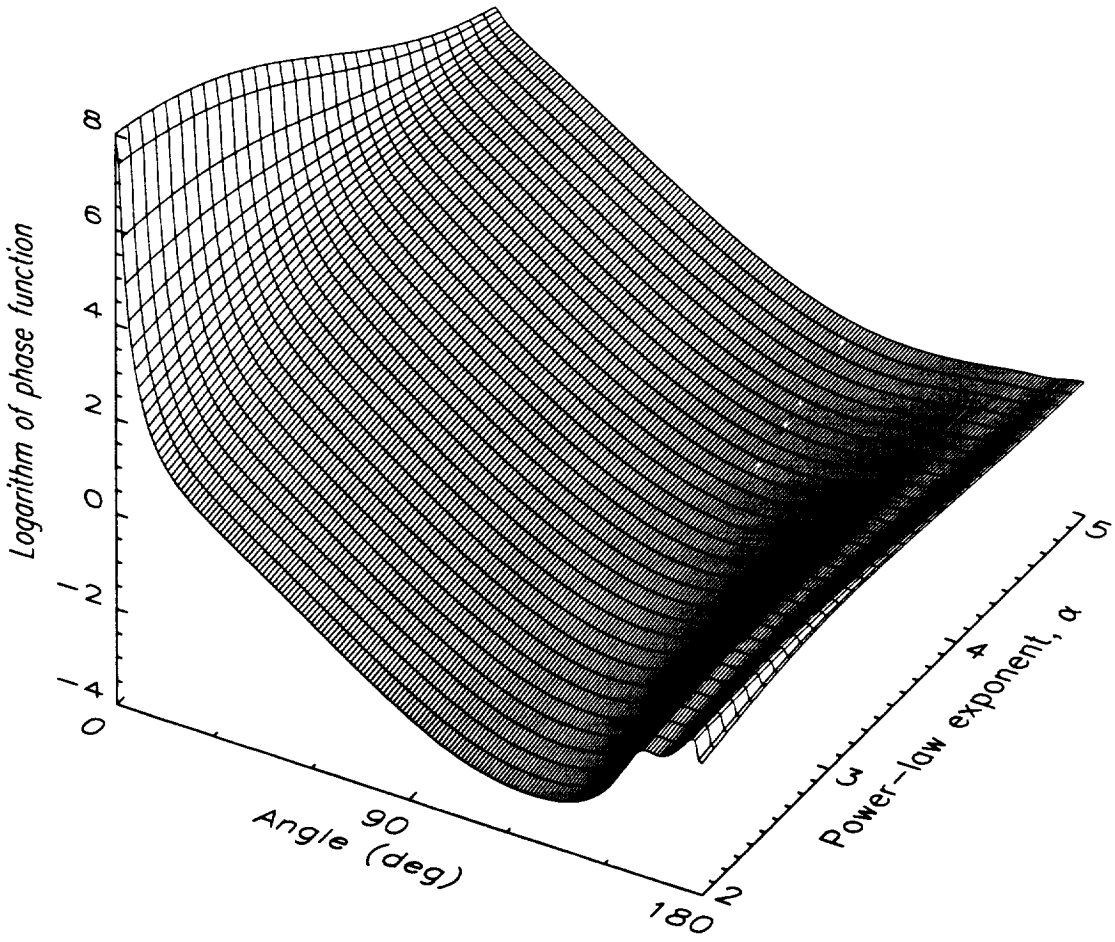
Logarithm of phase function
8
6
4
2
0
-2
-4
0
90
Angle (deg)
180
2
3
4
5
Power-law exponent, α

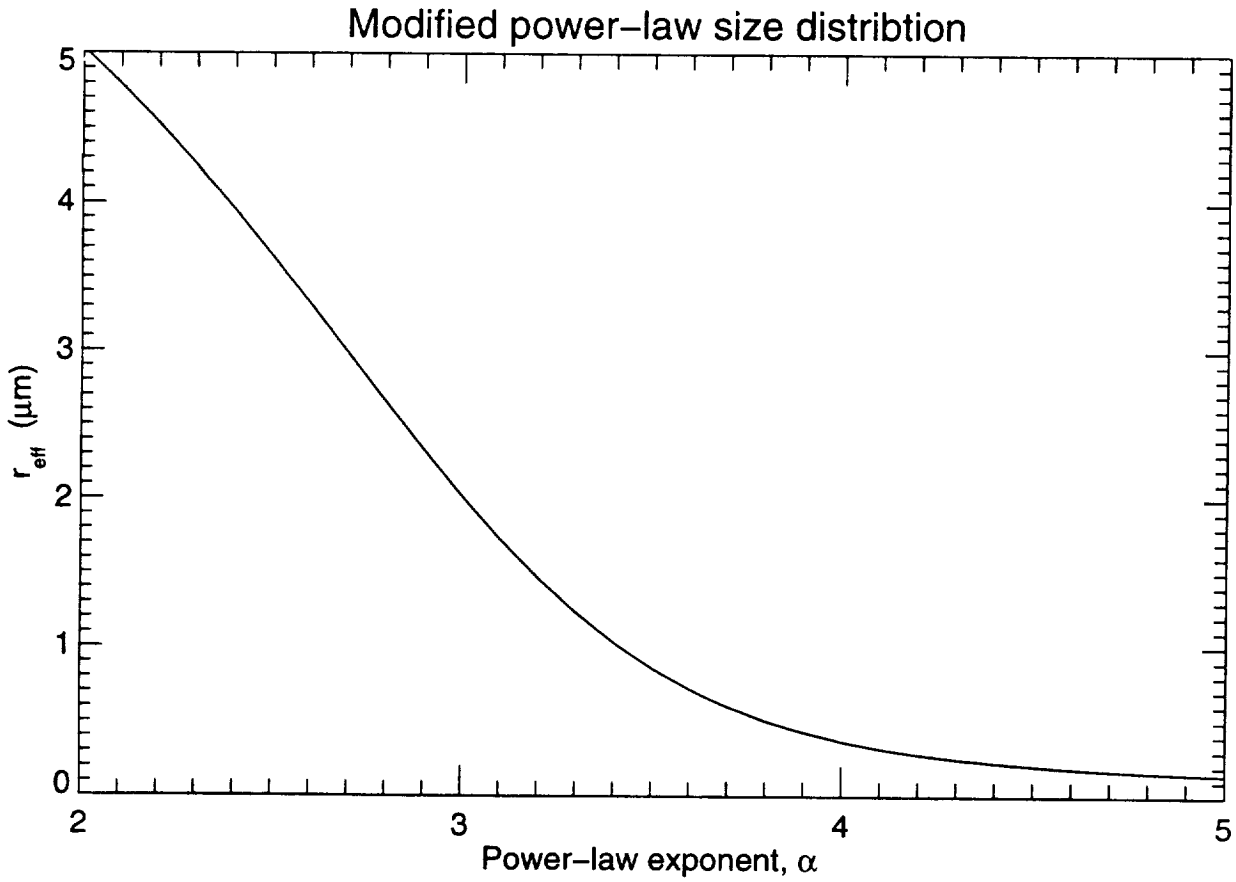
Modified power–law size distribtion
5
4
3
2
1
0
r_{eff} (μm)
2
3
4
5
Power–law exponent, α

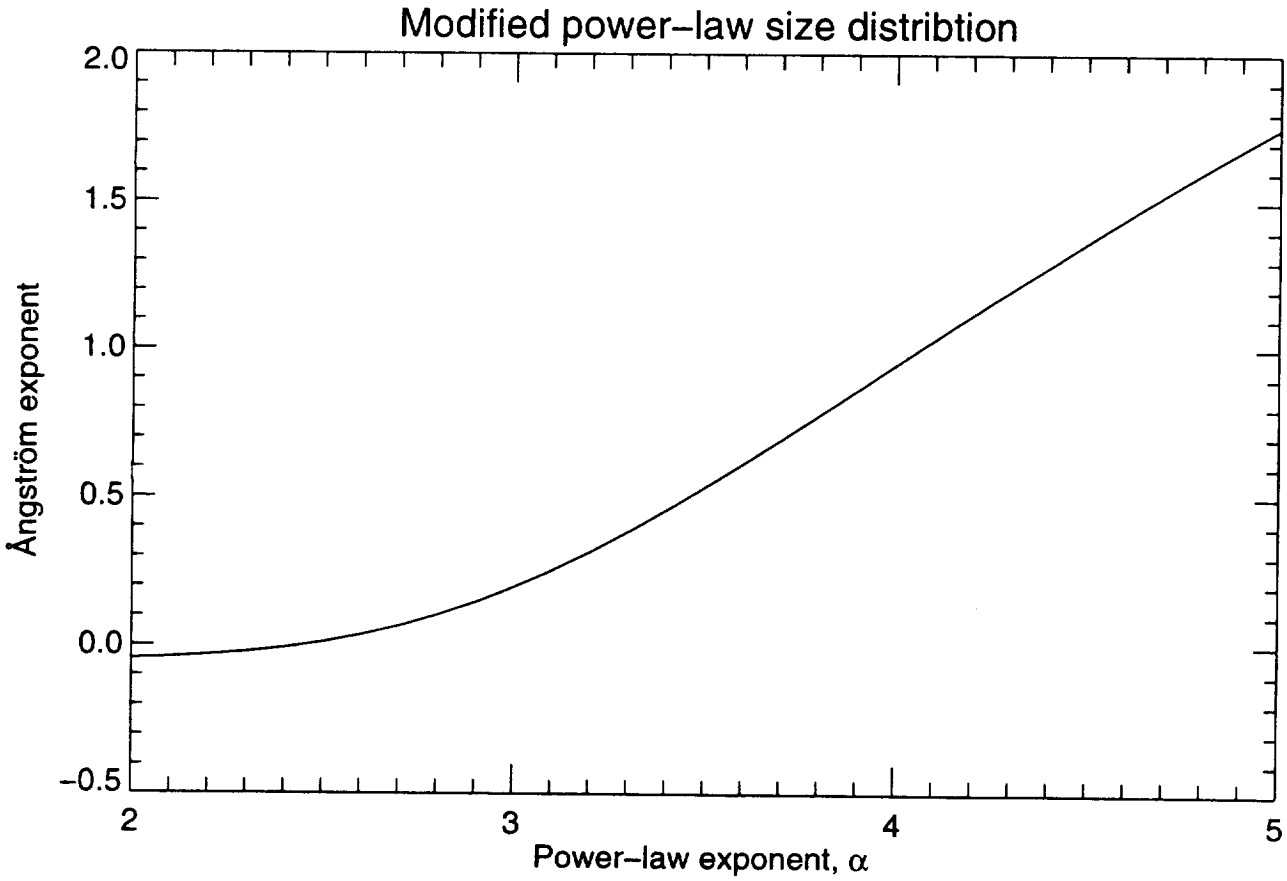
Modified power–law size distribtion
2.0
1.5
1.0
0.5
0.0
−0.5
Ångström exponent
2
3
4
5
Power–law exponent, α

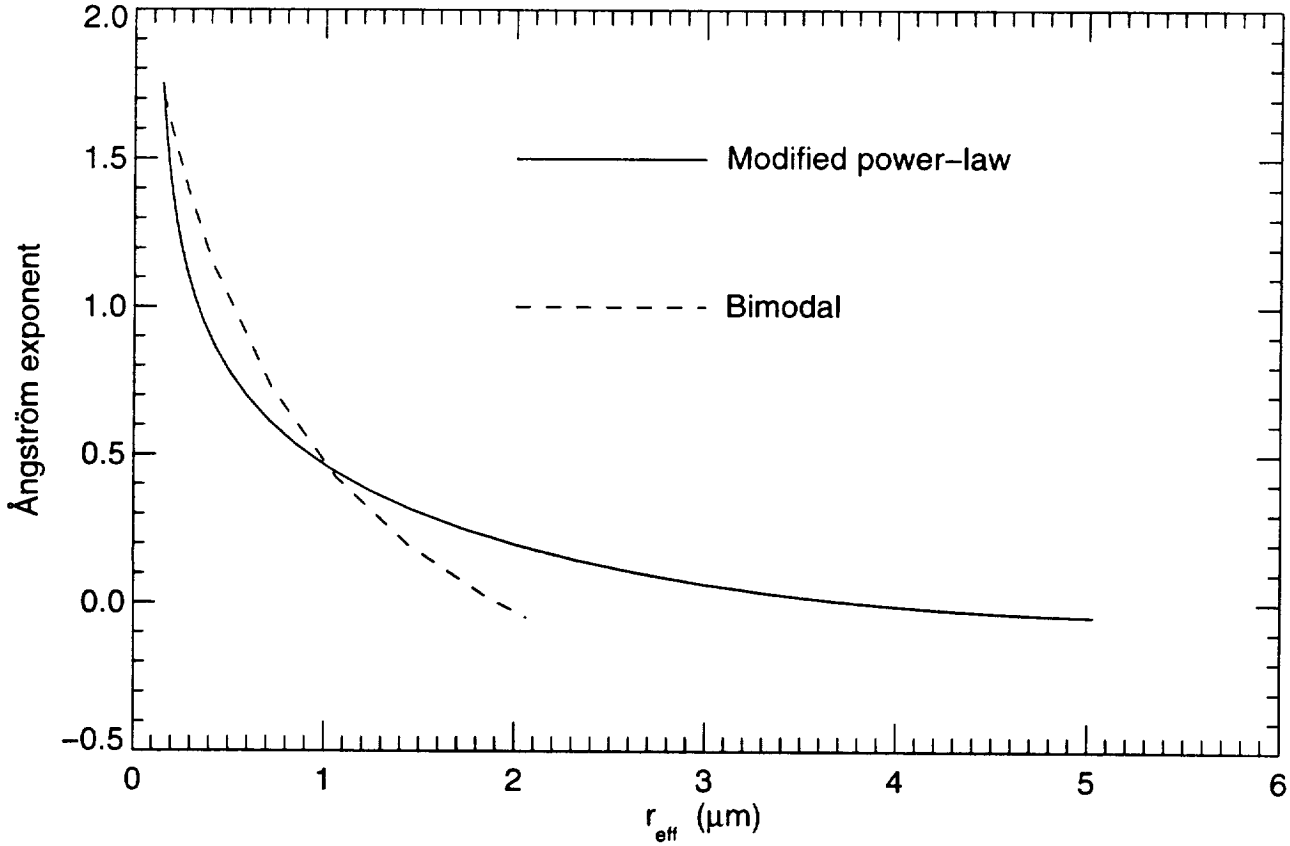
2.0
1.5
1.0
0.5
0.0
−0.5
Ångström exponent
0
1
2
3
4
5
6
r_{eff} (μm)
Modified power–law
Bimodal

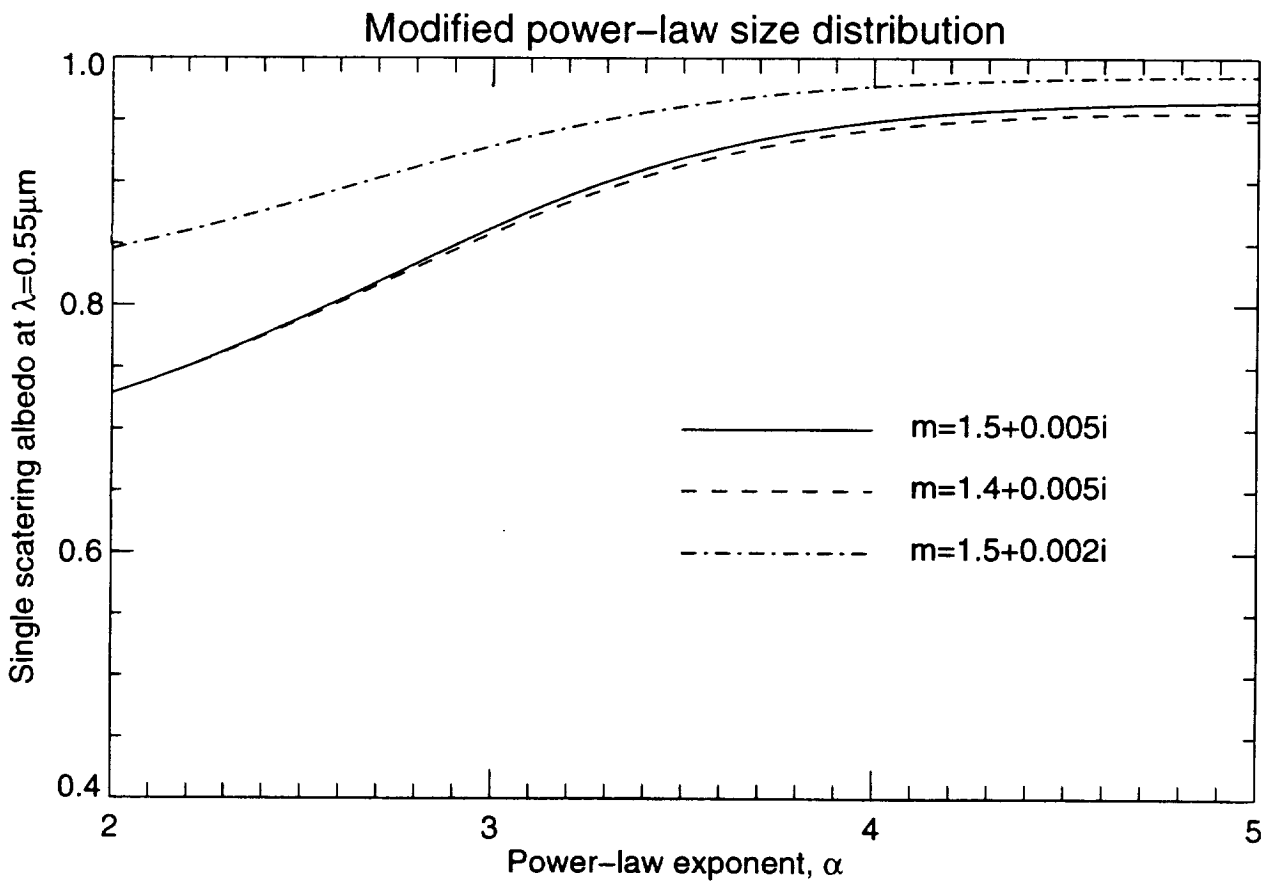
Modified power–law size distribution
Single scatering albedo at λ=0.55μm
1.0
0.8
0.6
0.4
2
3
4
5
Power–law exponent, α
m=1.5+0.005i
m=1.4+0.005i
m=1.5+0.002i

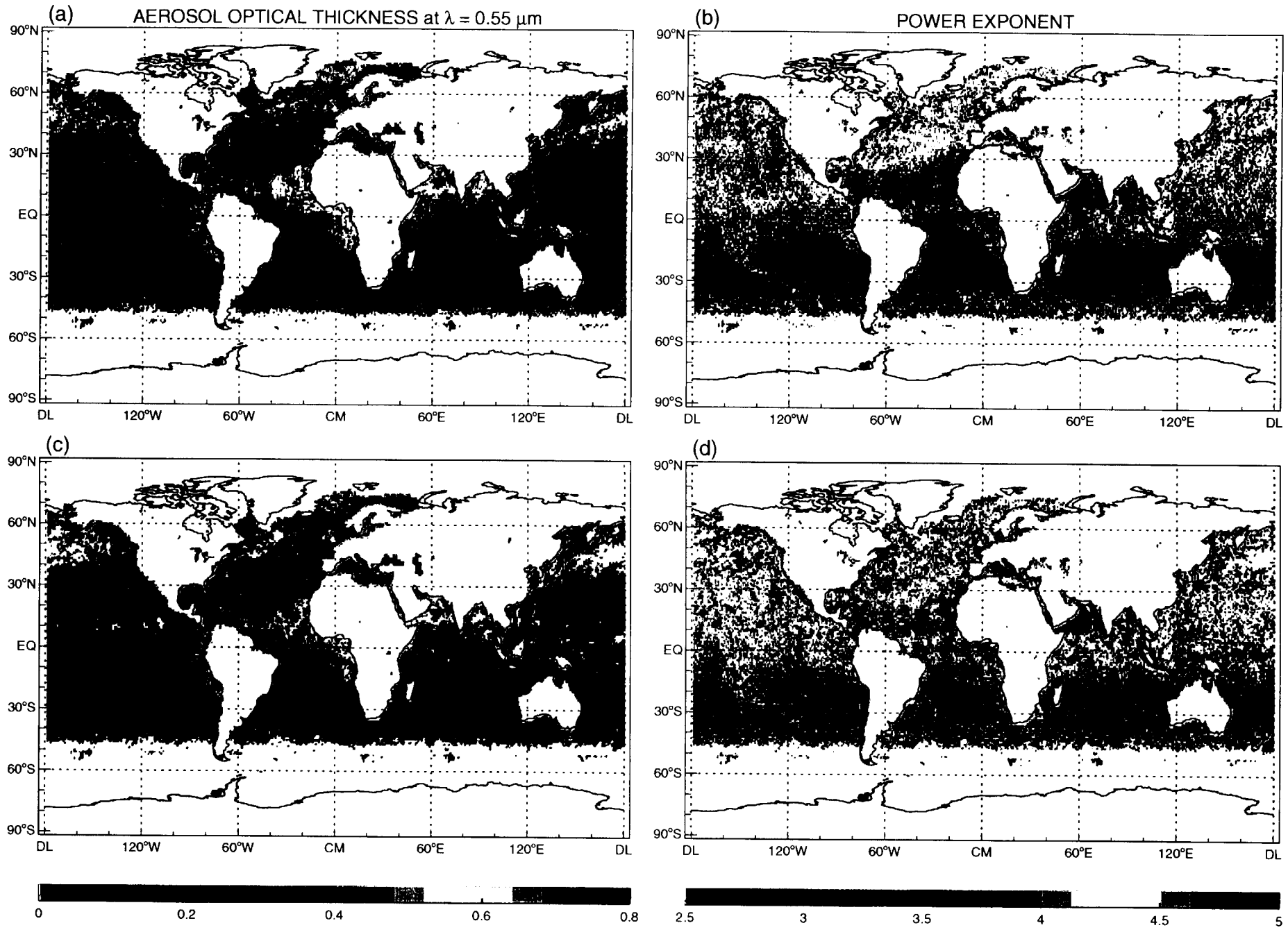
(a)
AEROSOL OPTICAL THICKNESS at λ = 0.55 μm
(b)
POWER EXPONENT
(c)
(d)
90°N
60°N
30°N
EQ
30°S
60°S
90°S
DL
120°W
60°W
CM
60°E
120°E
DL
0
0.2
0.4
0.6
0.8
2.5
3
3.5
4
4.5
5

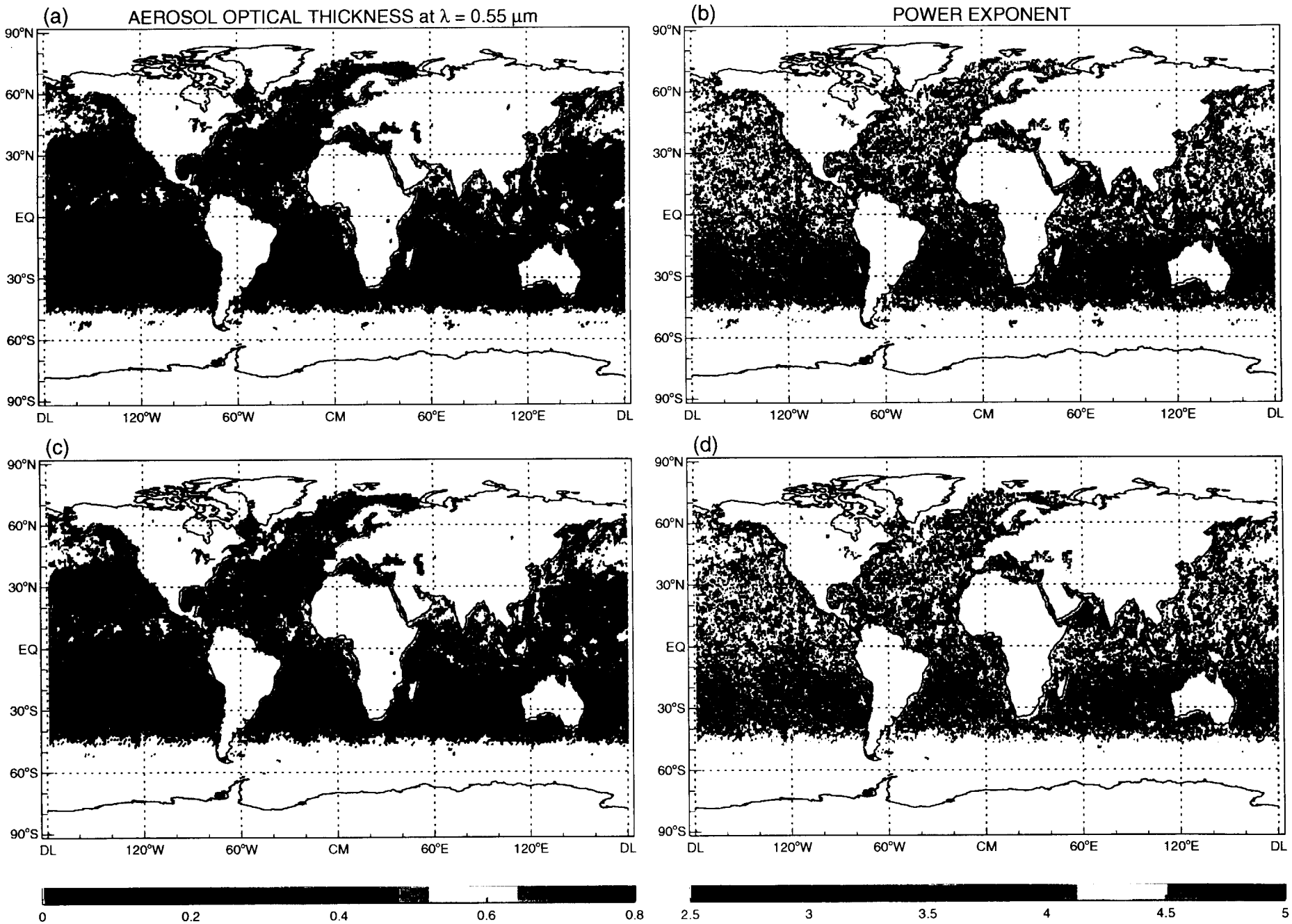
(a)
AEROSOL OPTICAL THICKNESS at λ = 0.55 μm
(b)
POWER EXPONENT
(c)
(d)
90°N
60°N
30°N
EQ
30°S
60°S
90°S
DL
120°W
60°W
CM
60°E
120°E
0
0.2
0.4
0.6
0.8
2.5
3
3.5
4
4.5
5

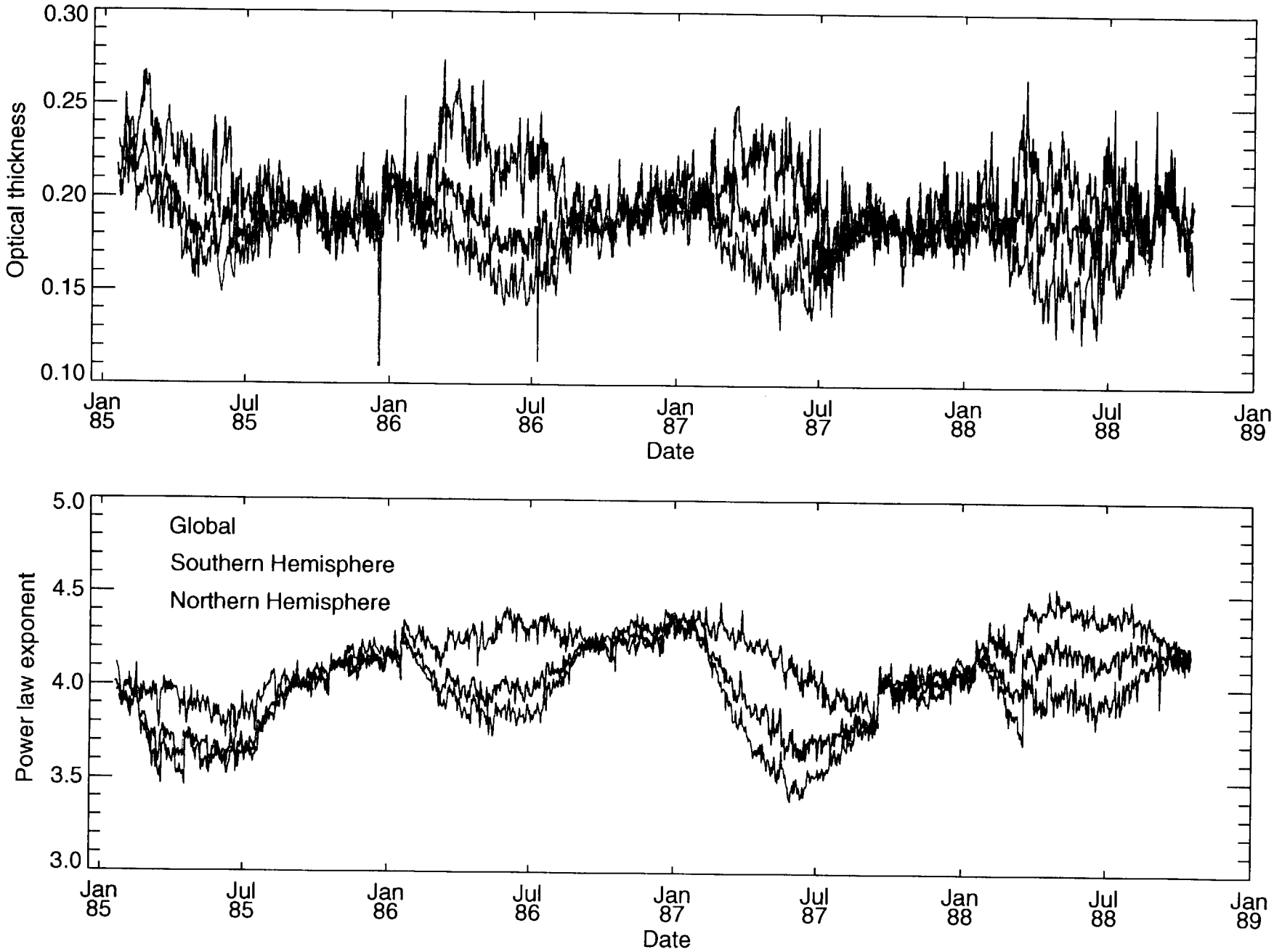
0.30
0.25
0.20
0.15
0.10
Optical thickness
Jan 85
Jul 85
Jan 86
Jul 86
Jan 87
Jul 87
Jan 88
Jul 88
Jan 89
Date
5.0
4.5
4.0
3.5
3.0
Power law exponent
Global
Southern Hemisphere
Northern Hemisphere
Jan 85
Jul 85
Jan 86
Jul 86
Jan 87
Jul 87
Jan 88
Jul 88
Jan 89
Date

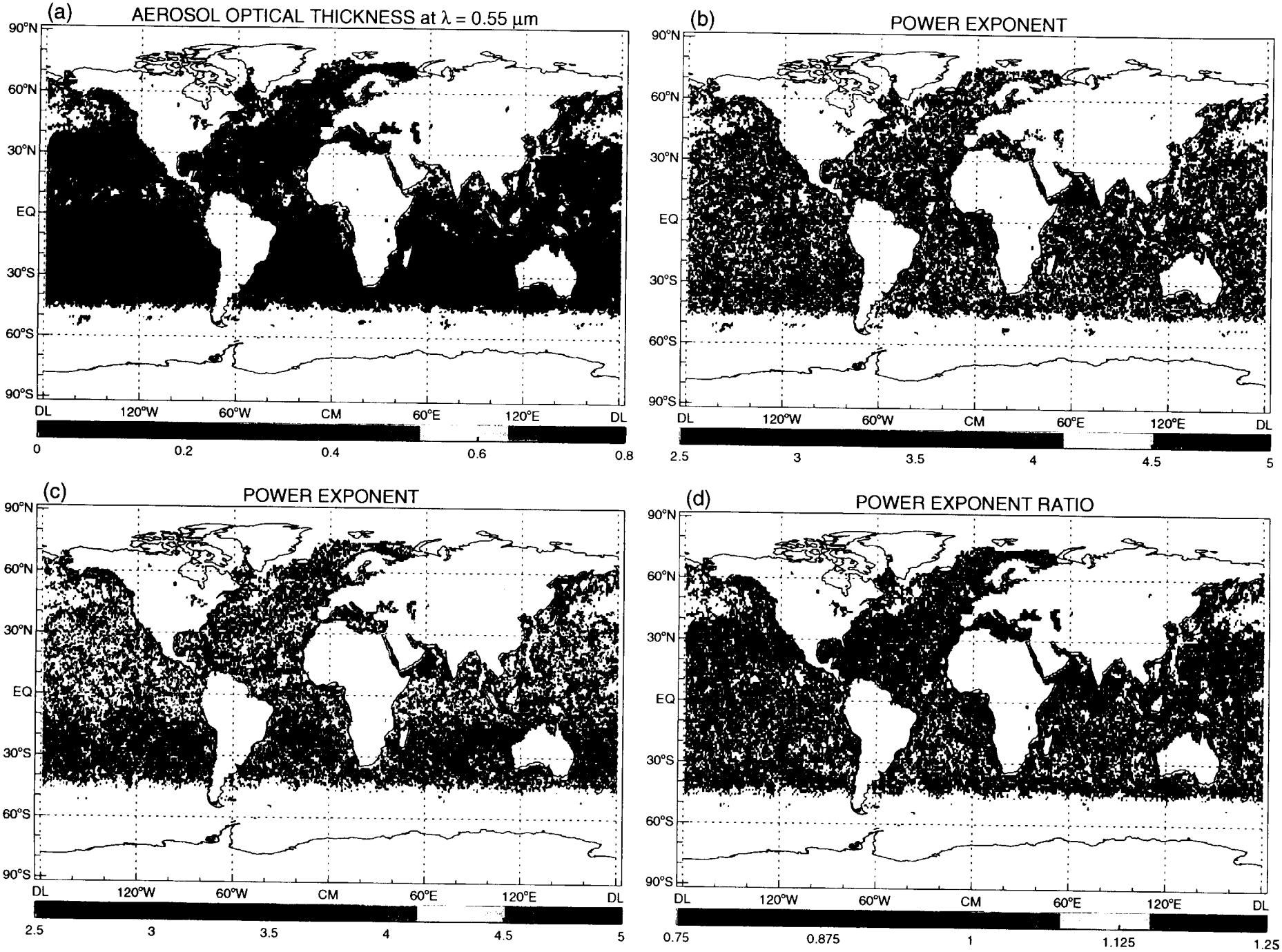
(a)
AEROSOL OPTICAL THICKNESS at λ = 0.55 μm
90°N
60°N
30°N
EQ
30°S
60°S
90°S
DL
120°W
60°W
CM
60°E
120°E
DL
0
0.2
0.4
0.6
0.8
(b)
POWER EXPONENT
2.5
3
3.5
4
4.5
5
(c)
POWER EXPONENT
(d)
POWER EXPONENT RATIO
0.75
0.875
1
1.125
1.25

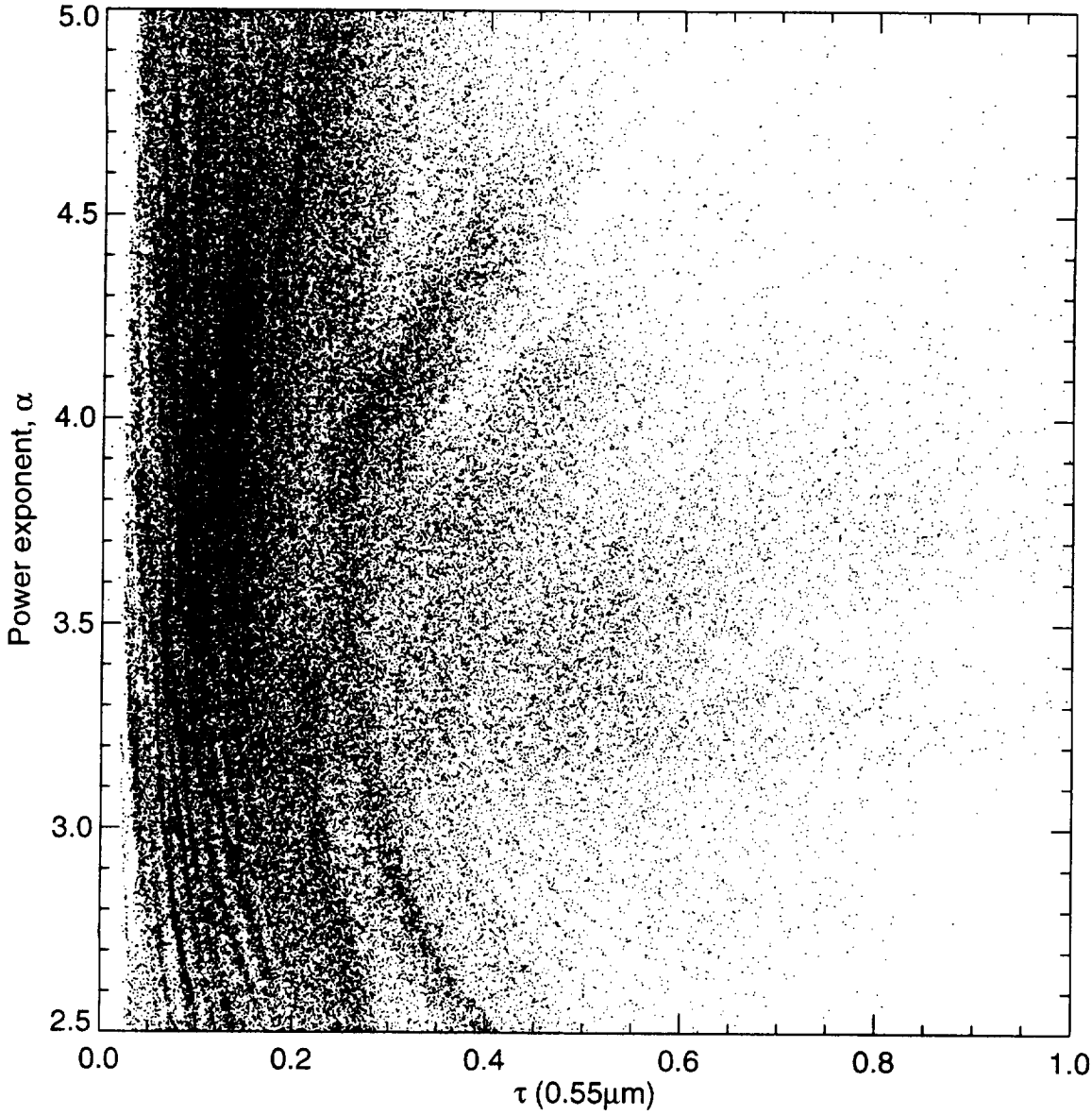
5.0
4.5
4.0
3.5
3.0
2.5
Power exponent, α
0.0
0.2
0.4
0.6
0.8
1.0
τ (0.55μm)

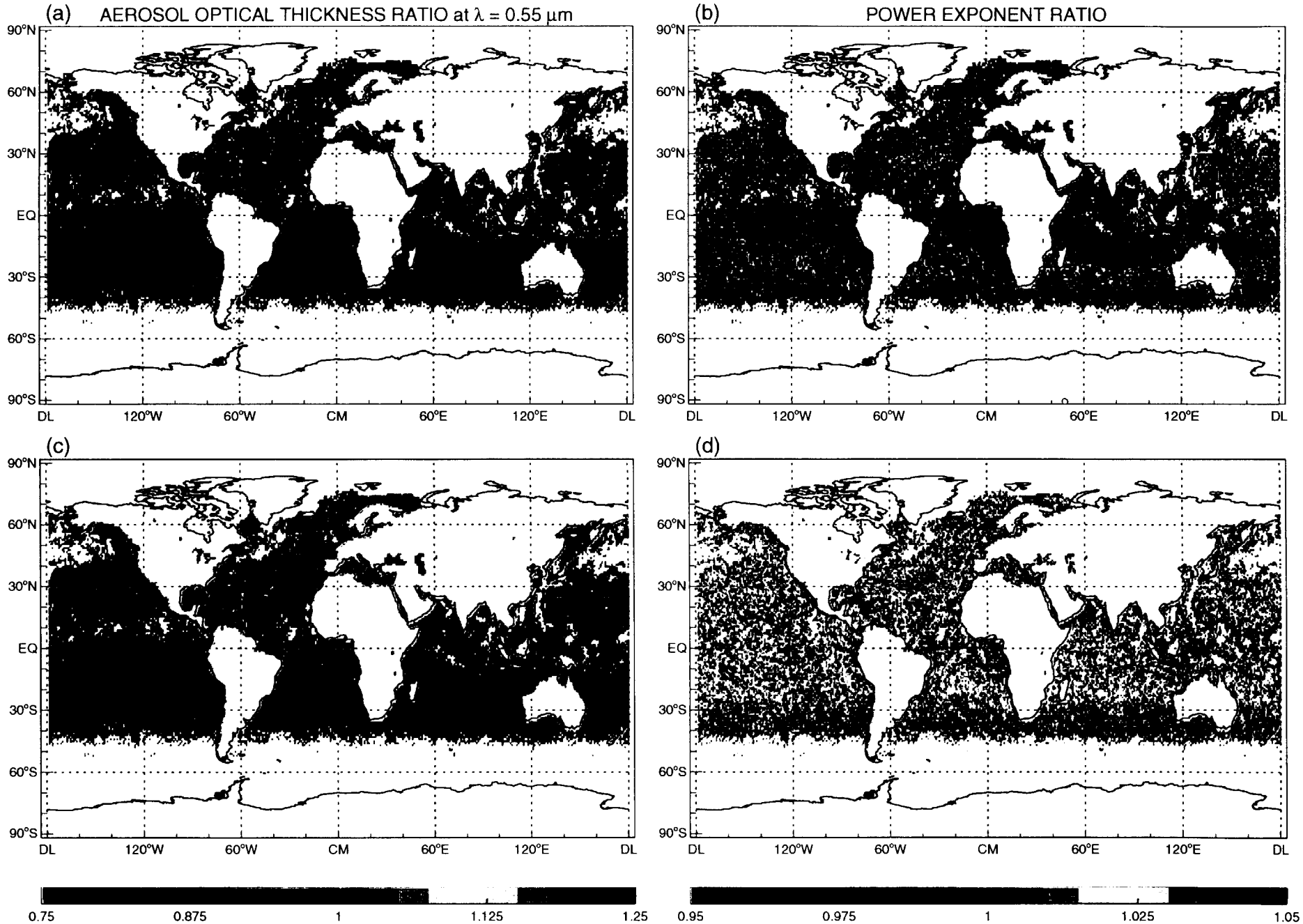
(a) AEROSOL OPTICAL THICKNESS RATIO at λ = 0.55 μm
(b) POWER EXPONENT RATIO
(c)
(d)
90°N
60°N
30°N
EQ
30°S
60°S
90°S
DL
120°W
60°W
CM
60°E
120°E
DL
0.75
0.875
1
1.125
1.25
0.95
0.975
1
1.025
1.05

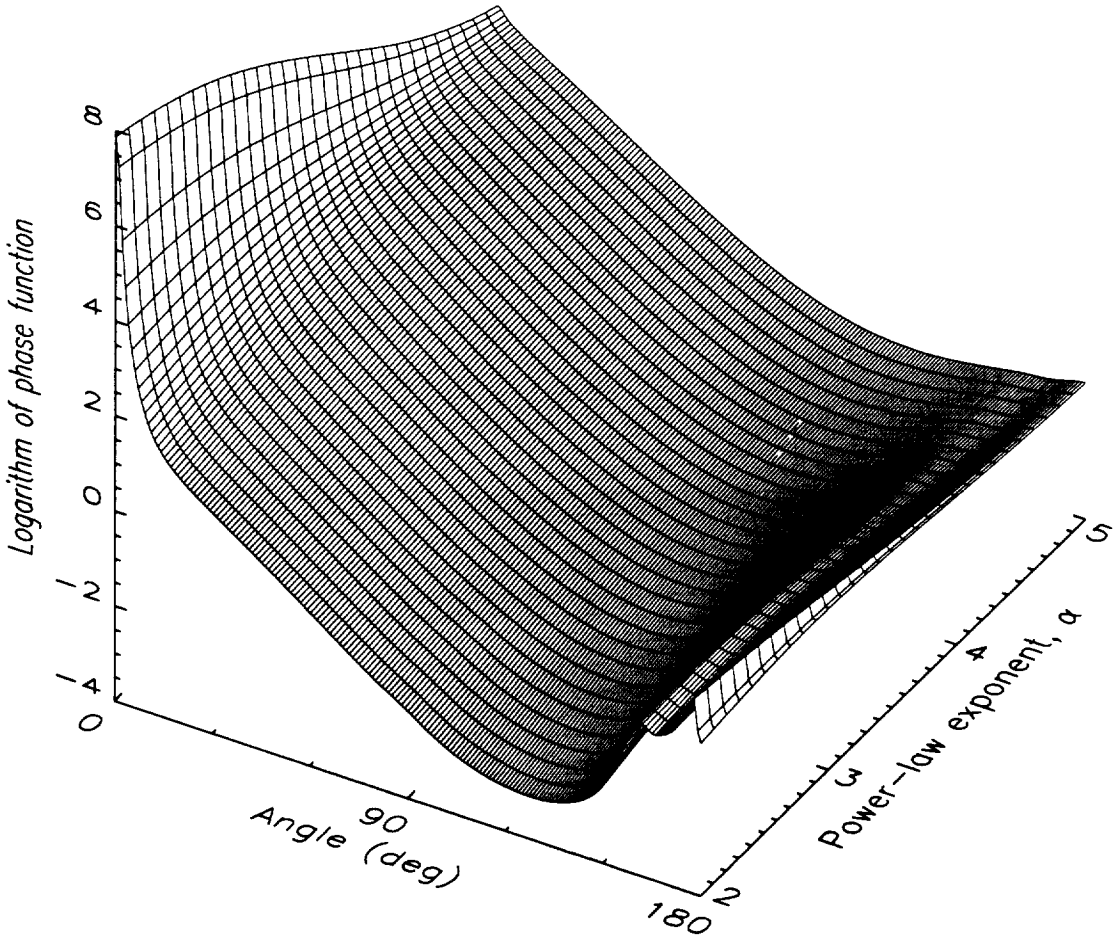
Logarithm of phase function
8
6
4
2
0
-2
-4
0
90
180
Angle (deg)
2
3
4
5
Power-law exponent, α

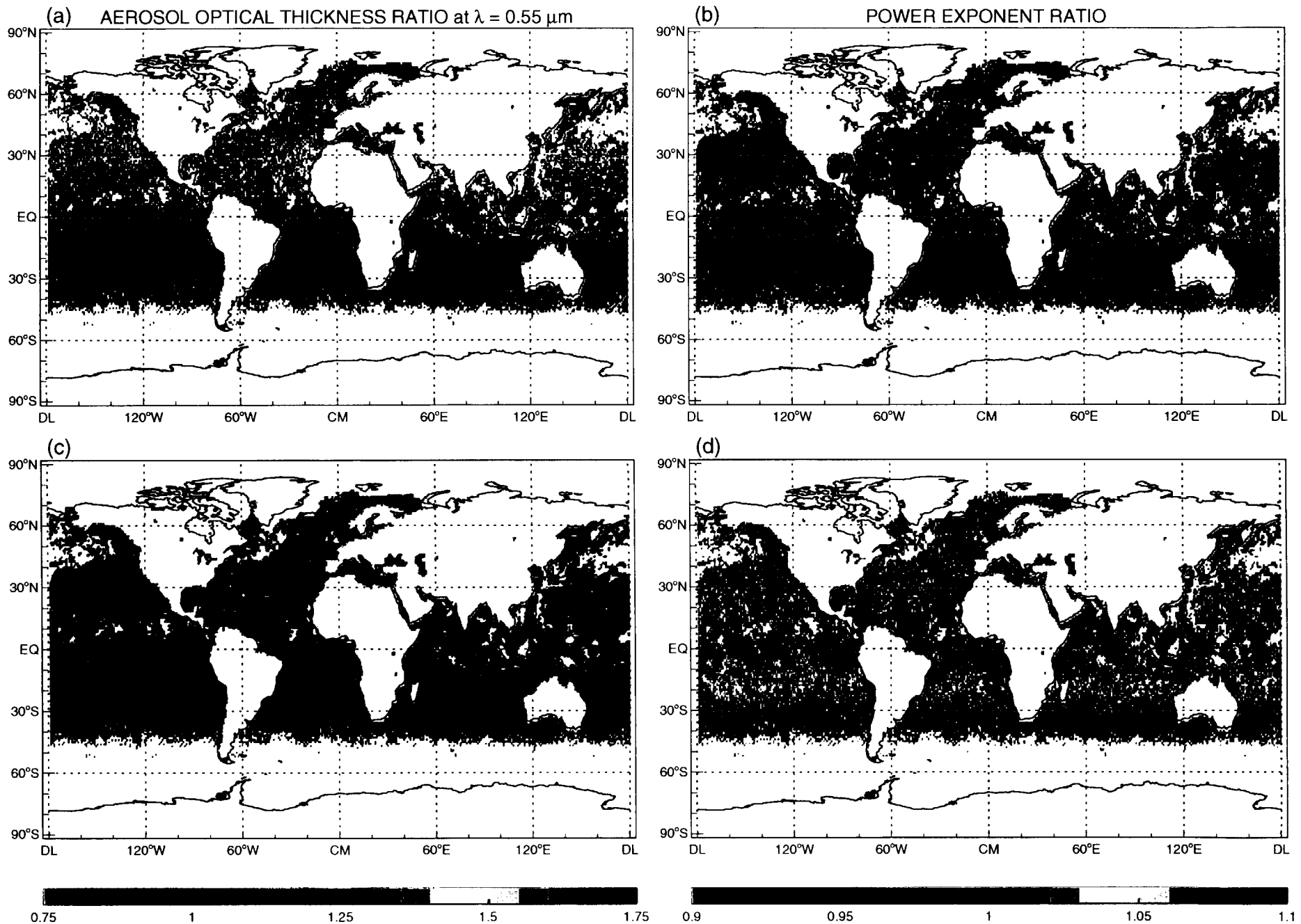
(a) AEROSOL OPTICAL THICKNESS RATIO at λ = 0.55 μm
(b) POWER EXPONENT RATIO
(c)
(d)
90°N
60°N
30°N
EQ
30°S
60°S
90°S
DL
120°W
60°W
CM
60°E
120°E
DL
0.75
1
1.25
1.5
1.75
0.9
0.95
1
1.05
1.1

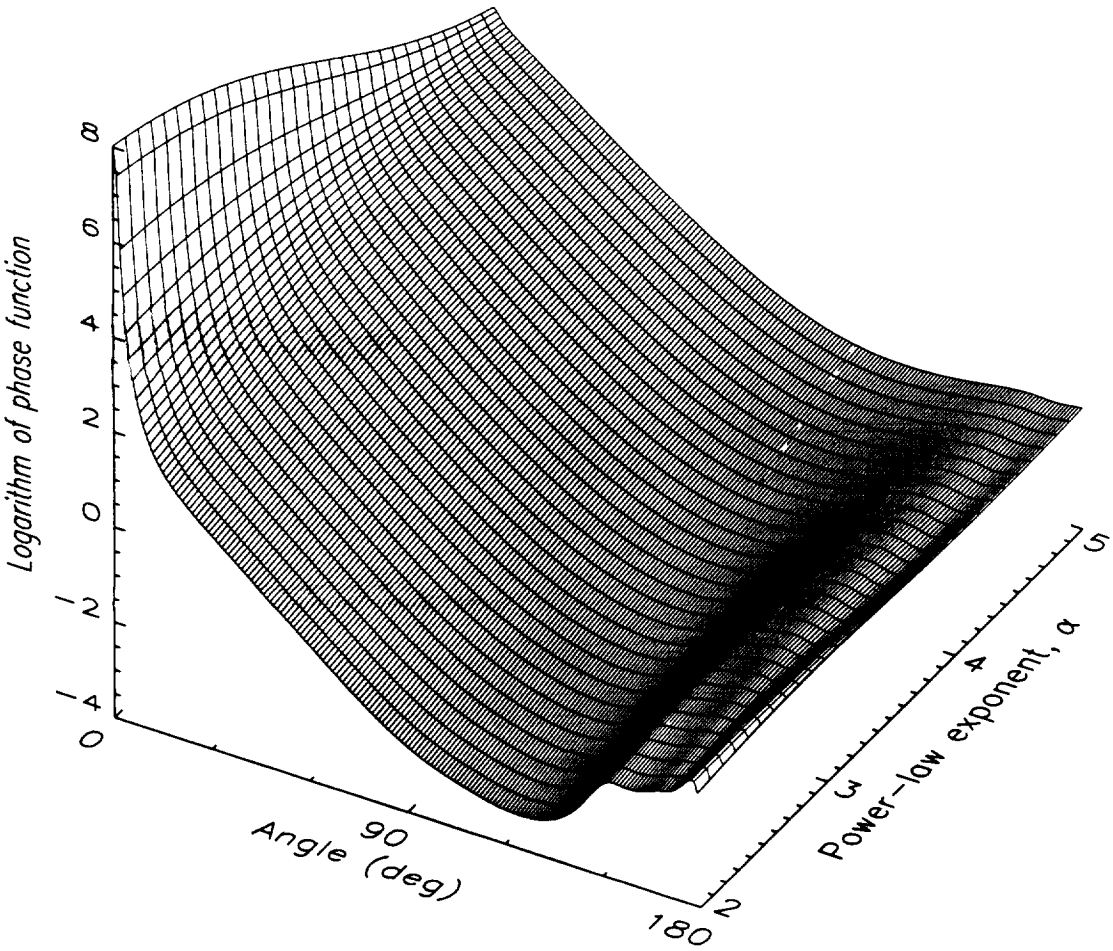
Logarithm of phase function
8
6
4
2
0
-2
-4
0
90
Angle (deg)
180
2
3
4
5
Power-law exponent, α

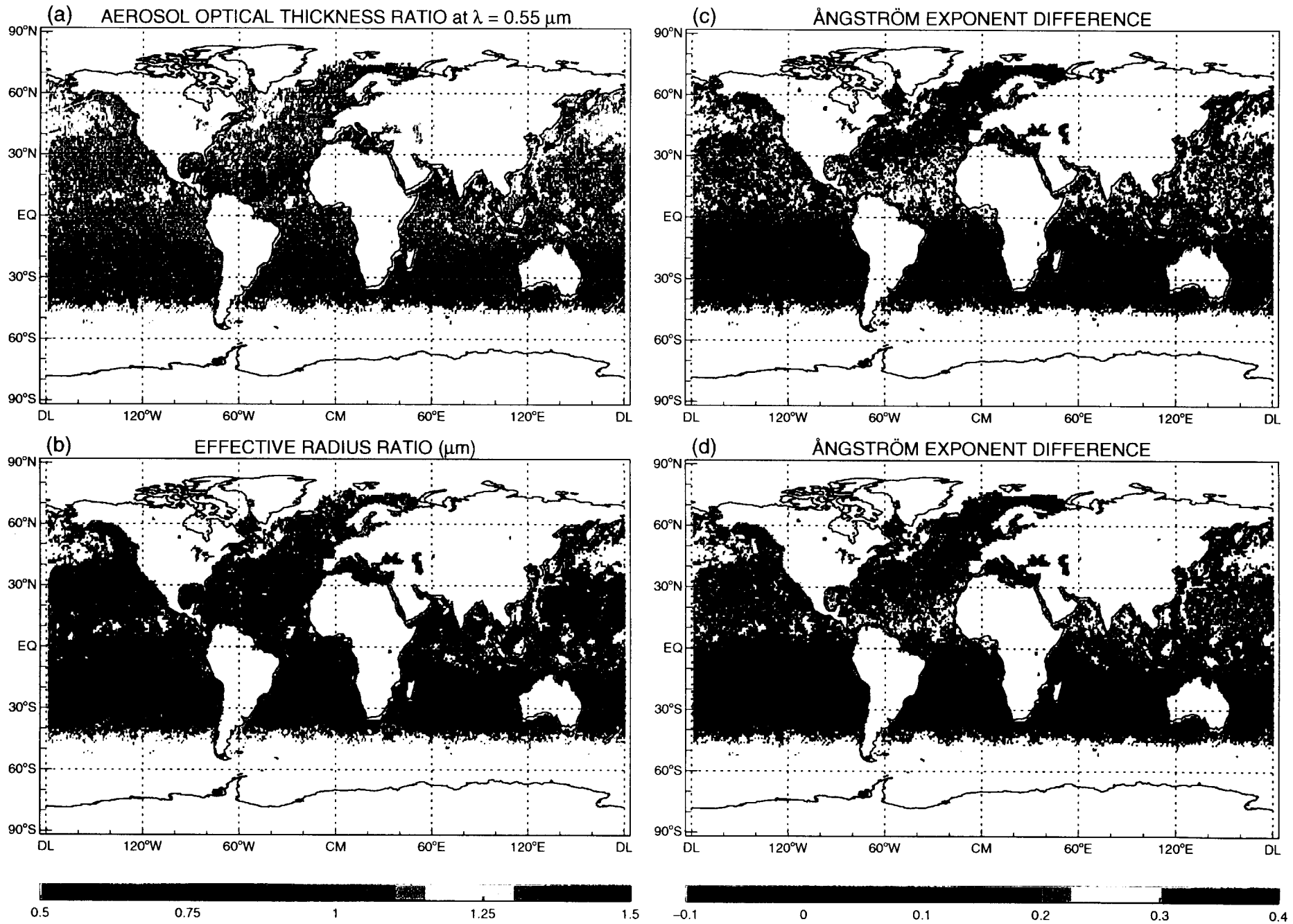
(a) AEROSOL OPTICAL THICKNESS RATIO at λ = 0.55 μm
(c) ÅNGSTRÖM EXPONENT DIFFERENCE
(b) EFFECTIVE RADIUS RATIO (μm)
(d) ÅNGSTRÖM EXPONENT DIFFERENCE
90°N
60°N
30°N
EQ
30°S
60°S
90°S
DL
120°W
60°W
CM
60°E
120°E
DL
0.5
0.75
1
1.25
1.5
−0.1
0
0.1
0.2
0.3
0.4

51

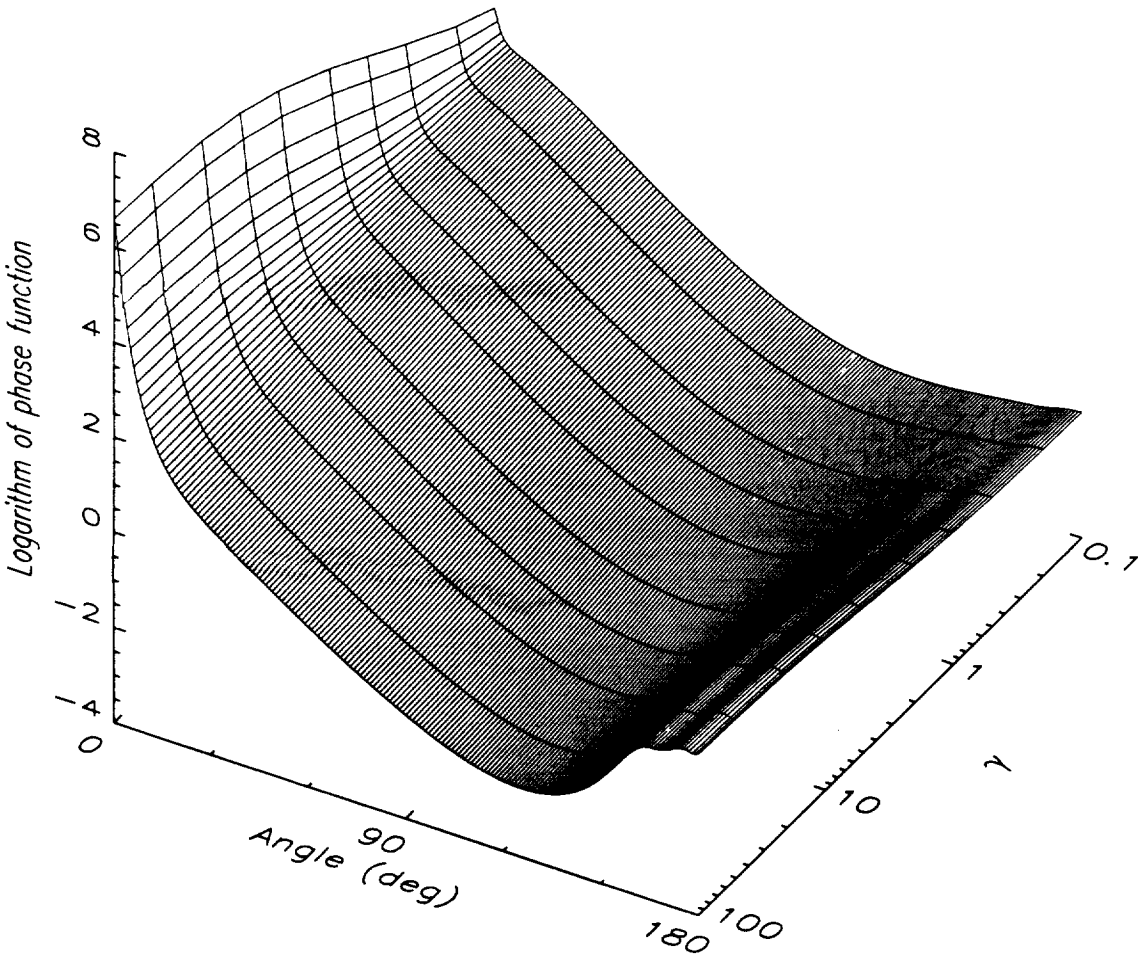
Logarithm of phase function
8
6
4
2
0
-2
-4
0
90
Angle (deg)
180
0.1
1
10
100
γ

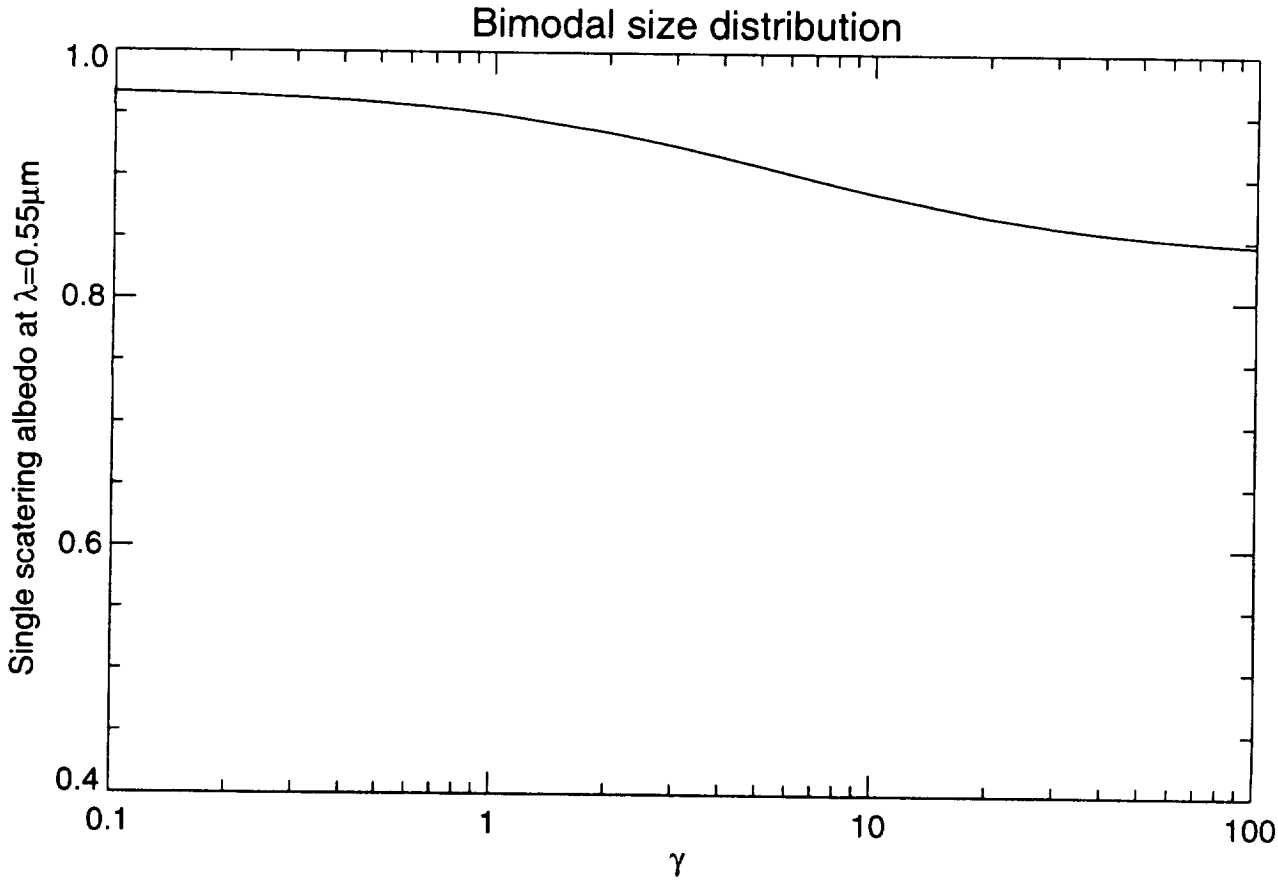
Bimodal size distribution
Single scatering albedo at λ=0.55μm
1.0
0.8
0.6
0.4
0.1
1
10
100
γ

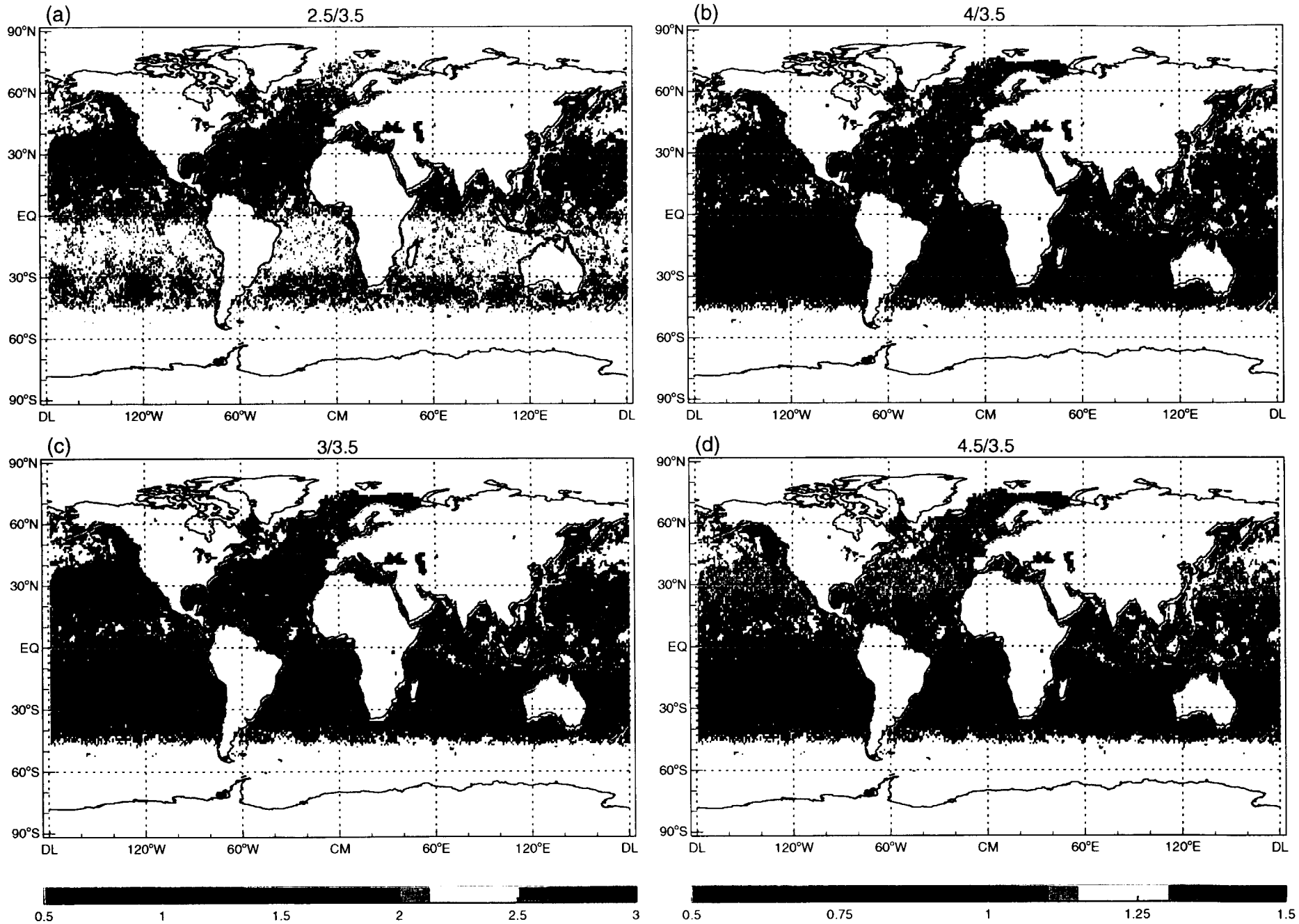
(a)
2.5/3.5
(b)
4/3.5
(c)
3/3.5
(d)
4.5/3.5
90°N
60°N
30°N
EQ
30°S
60°S
90°S
DL
120°W
60°W
CM
60°E
120°E
0.5
1
1.5
2
2.5
3
0.5
0.75
1
1.25
1.5

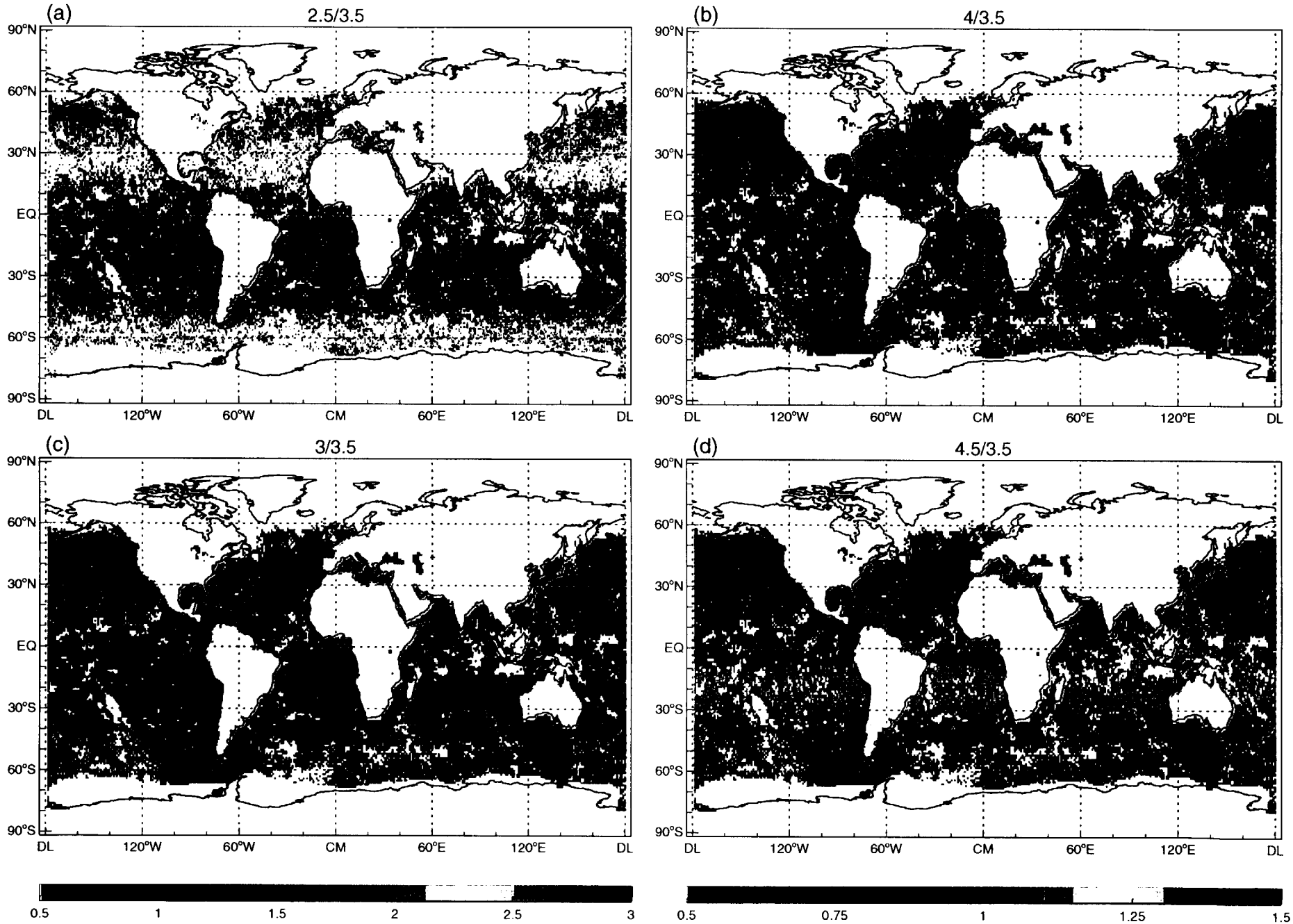
(a)
2.5/3.5
(b)
4/3.5
(c)
3/3.5
(d)
4.5/3.5
90°N
60°N
30°N
EQ
30°S
60°S
90°S
DL
120°W
60°W
CM
60°E
120°E
DL
0.5
1
1.5
2
2.5
3
0.5
0.75
1
1.25
1.5